# Site-Directed Mutagenesis of *Thermosynechococcus elongatus* Photosystem II: The $O_2$-Evolving Enzyme Lacking the Redox-Active Tyrosine D

Miwa Sugiura,*,‡,§ Fabrice Rappaport,|| Klaus Brettel,‡ Takumi Noguchi,⊥ A. William Rutherford,‡ and Alain Boussac*,‡

*Service de Bioénergétique, DBJC, URA CNRS 2096, CEA Saclay, 91191 Gif-sur-Yvette, France, Department of Applied Biological Chemistry, Faculty of Agriculture, Osaka Prefecture University, 1-1 Gakuen-cho, Sakai, Osaka 599-8531, Japan, Institut de Biologie Physico-Chimique, CNRS, UPR 1261, 13 rue Pierre et Marie Curie, 75005 Paris, France, and Institute of Materials Science, University of Tsukuba, Tsukuba, Ibaraki 305-8573, Japan*

*Received June 18, 2004; Revised Manuscript Received August 19, 2004*

ABSTRACT: Site-directed mutagenesis in the photosystem II (PSII) oxygen-evolving enzyme was achieved in the thermophilic cyanobacterium *Thermosynechococcus elongatus*. PSII from this species is the focus of attention because its robustness makes it suitable for enzymological and biophysical studies. PSII, which lacks the redox-active tyrosine $Tyr_D$, was engineered by substituting a phenylalanine for tyrosine 160 of the D2 protein. An aim of this work was to engineer a mutant for spectroscopy, in particular, for EPR, on the active enzyme. The $Tyr_D^{\bullet}$ EPR signal was monitored in whole cells (i) to control the expression level of the two genes (*psbD₁* and *psbD₂*) encoding D2 and (ii) to assess the success of the mutagenesis. Both *psbD₁* and *psbD₂* could be expressed, and recombination occurred between them. The D2-Y160F mutation was introduced into *psbD₁* after *psbD₂* was deleted and a His-tag was attached to the CP43 protein. The effects of the Y160F mutation were characterized in cells, thylakoids, and isolated PSII. The efficiency of enzyme function under the conditions tested was unaffected. The distribution and lifetime of the redox states ($S_n$ states) of the enzyme cycle were modified, with more $S_0$ in the dark and no rapid decay phase of $S_3$. Although not previously reported, these effects were expected because $Tyr_D^{\bullet}$ is able to oxidize $S_0$ and $Tyr_D$ is able to reduce $S_2$ and $S_3$. Slight changes in the difference spectra in the visible and infrared recorded upon the formation and reduction of the chlorophyll cation $P_{680}^{+}$ and kinetic measurements of $P_{680}^{+}$ reduction indicated minor structural perturbations, perhaps in the hydrogen-bonding network linking $Tyr_D$ and $P_{680}$, rather than electrostatic changes associated with the loss of a charge from $Tyr_D^{\bullet}(H^+)$. We show here that this fully active preparation can provide spectra from the $Mn_4CaO_4$ complex and associated radical species uncontaminated by $Tyr_D^{\bullet}$.

Photosystem II (PSII)[1] catalyses light-driven water oxidation and plastoquinone reduction in cyanobacteria, algae, and plants (*1*−*6*). Water oxidation takes place at a $Mn_4CaO_4$ cluster, a structural model for which has been recently proposed based on X-ray crystallography (*7*). This model is largely consistent with earlier spectroscopic work (*8*, *9*). PSII is a membrane-spanning complex constituted of at least 16 subunits including the central D1/D2 dimer that is surrounded by CP43 and CP47, cytochrome *b*559, 11 small polypeptides, and 3 extrinsic proteins, including the cytochrome *c*550. PSII contains chlorophylls (Chls), carotenoids, pheophytins, plastoquinones, a non-heme iron, a calcium, and 4 manganese ions. Although the deduced amino acid sequences of D1 and D2 share a rather low homology (30%) (*10*, *11*), the important amino acid residues such as those that act as ligands to the cofactors are conserved. The central Chl molecules ($P_{D1}$ and $P_{D2}$, $Chl_{D1}$ and $Chl_{D2}$), pheophytins ($Pheo_{D1}$ and $Pheo_{D2}$), plastoquinones ($Q_B$ and $Q_A$), peripheral Chls ($Chl_{ZD1}$ and $Chl_{ZD2}$), and two redox-active tyrosines ($Tyr_Z$ and $Tyr_D$) occupy symmetrical position on the D1 and D2 proteins and are hydrogen-bonded to D1-H190 and D2-H189, respectively (*5*−*7*, *12*−*15*), while the $Mn_4CaO_4$ cluster is located in D1 (*1*−*7*).

The absorption of a photon results in a charge separation between one of the central Chl molecules and a pheophytin molecule, $Pheo_{D1}$. The pheophytin anion transfers the electron to a quinone, $Q_A$. $P_{680}^{+}$, where the cation is shared through a redox equilibrium over $P_{D1}$ and $P_{D2}$ (*16*, *17*), is reduced by a tyrosine residue, $Tyr_Z$. $Tyr_Z^{\bullet}$ is in turn reduced by the $Mn_4CaO_4$ cluster. During the enzyme cycle driven by

* To whom correspondence should be addressed: E-mail: miwa@biochem.osakafu-u.ac.jp. Telephone: 81 72 254 9451. Fax: 81 72 254 9918 (M.S.); E-mail: alain.boussac@cea.fr. Telephone: 33 1 69 08 72 06. Fax: 33 1 69 08 87 17 (A.B.).

‡ Service de Bioénergétique, DBJC.

§ Osaka Prefecture University.

|| Institut de Biologie Physico-Chimique.

⊥ University of Tsukuba.

[1] Abbreviations: PSII, photosystem II; Chl, chlorophyll; EPR, electron paramagnetic resonance; cw, continuous wave; FTIR, Fourier transform infrared; Mes, 2-(*N*-morpholino)ethanesulfonic acid; DCBQ, 2,6-dichloro-*p*-benzoquinone; Nd:YAG, neodymium:yttriumaluminum garnet; $\beta$DM, *n*-dodecyl-$\beta$-maltoside; $P_{680}$, photooxidizable Chl of PSII; $P_{D1}$ and $P_{D2}$, two central Chls bound to polypeptide D1 and D2, respectively; $Tyr_Z$, tyrosine acting as the electron donor to $P_{680}^{+}$; $Tyr_D$, tyrosine acting as a side-path electron donor of PSII; PEG, poly(ethylene glycol); Cm, chloramphenicol; Km, kanamycin; PPBQ, phenyl-*p*-benzoquinone; WT′, wild-type that has a His-tag on the C terminus of CP43; SOD; superoxide dismutase.

10.1021/bi048732h CCC: $27.50 
Published on Web 10/02/2004

sequential light-induced charge separations, the oxidizing side of PSII goes through five different redox states that are denoted $S_n$, *n* varying from 0 to 4 (18). Oxygen is released during the $S_3-S_0$ transition, in which $S_4$ is a transient state (*1*−*6*, *18*).

The recent structural models of PSII based on X-ray crystallography have come from the thermophilic cyanobacterium *Thermosynechoccocus elongatus* (*7*, *19*, *20*). The enzyme in this species is very robust, and this makes it particularly suited not only for crystallography (*7*, *19*) but also for spectroscopic and enzymological studies (*21*−*28*). This cyanobacterium, however, is less well-suited for molecular biological studies because of, for example, (i) difficulties in the introduction of exogenous DNA in the chromosome, (ii) the presence of processes of recombination between the introduced gene and genomic DNA, and (iii) the very slow segregation of mutated cells in culture on plates. While it has been possible to generate a histidine-tagged strain that has allowed more efficient isolation of the enzyme (*29*), up to now, no single amino acid site-directed mutagenesis of the PSII reaction center has been reported. Here, we set out to produce a site-directed mutant in the PSII reaction center of *T. elongatus*.

Our aim was to develop procedures to produce mutants in *T. elongatus* and then to isolate mutated PSII in which the $Mn_4CaO_4$ cluster remains completely intact. The target chosen was the replacement of the redox-active tyrosine $Tyr_D$ with phenylalanine (Y160F) in the D2 protein. There were several reasons for this choice: (i) The mutant has been constructed before in mesophilic species (*30*, *31*), and the enzyme was still functional in whole cells; thus, we expected photosynthetic growth to be largely unaffected, a prerequisite in *T. elongatus*, which is not able to grow on glucose unlike *Synechocystis* sp. PCC 6803. (ii) The stable radical $Tyr_D^•$ could be monitored by electron paramagnetic resonance (EPR) in whole cells, and therefore the progress of the molecular biological work could be easily monitored. (iii) The role of $Tyr_D$ is still being debated, reviewed in ref *32* and see below. (iv) An isolated, fully intact, $Tyr_D$-less enzyme would represent the ideal and long-wished-for material for many spectroscopic studies of the enzyme. The kinetically competent $Tyr_Z$, which is at the heart of the active site (*33*), can potentially be confused with $Tyr_D$. The problem is particularly marked in EPR studies. Although EPR has played a leading role in understanding the structure and function of PSII, all studies of the intact enzyme have had to deal with the fact that $Tyr_D^•$ contaminates the spectra. This can obscure and confuse studies of $Tyr_Z^•$ or any other radical process in the active enzyme.

Despite structural similarities, $Tyr_Z$ and $Tyr_D$ have different redox potentials, with the $Tyr_Z^•/Tyr_Z$ couple thought to be close to 1 V and the $Tyr_D^•/Tyr_D$ couple close to 0.75 V (*34*). The kinetic properties of $Tyr_Z$ depend on several factors such as the integrity and redox state of the $Mn_4CaO_4$ cluster and the presence of the calcium ion. In oxygen-evolving PSII, electron donation from $Tyr_Z$ to $P_{680}^+$ occurs in the tens of nanoseconds to microseconds time scale and depends on the redox state of the $Mn_4CaO_4$ cluster (*35*−*37*). Reduction of $Tyr_Z^•$ by the $Mn_4CaO_4$ cluster occurs in the tens of microseconds to milliseconds time scale depending on the redox state of the $Mn_4CaO_4$ cluster (*40*, *41*). $Tyr_D^•$ is stable and decays in days in the intact enzyme (*32*).

$Tyr_D$ is present in all species so far investigated, yet its removal by site-directed mutagenesis seemed only to slow cell growth (*30*, *31*), while not greatly influencing the enzyme function. A role for $Tyr_D$ in so-called "photo-activation", the process by which $Mn^{II}$ is bound, oxidized, and assembled as the $Mn_4CaO_4$ cluster, was suggested (*31*, *40*), and experimental evidence confirming such a role was obtained recently (*41*).

In the oxygen-evolving enzyme, $Tyr_D$ has a redox role. It can donate electrons to the $Mn_4CaO_4$ cluster when in the long-living high redox states, $S_2$ and $S_3$ (*42*, *43*), and $Tyr_D^•$ is able to oxidize the lowest redox state of the enzyme cycle, converting $S_0$ to $S_1$ (*40*) and also more reduced forms of the $Mn_4CaO_4$ cluster (*44*). These redox reactions are thought to occur through the equilibrium $Tyr_D^• + P_{680} \leftrightarrow Tyr_D + P_{680}^+$.

An electrostatic role for $Tyr_D$ might occur through the generation of a proton upon radical formation, $Tyr_D^•(H^+)$ (*32*), with the proton located on a close-by protonatable group such as D2-H189 (*13*, *14*). This proton would have an electrostatic influence on $P_{680}^+$, increasing its potential and displacing the redox equilibrium, $P_{D1}^+P_{D2} \leftrightarrow P_{D1}P_{D2}^+$, to the left, thereby accelerating the rate of $Tyr_Z$ oxidation, reviewed in refs *17* and *32*. Studies on the electrostatic role of $Tyr_D^•$, however, were done in Mn-depleted PSII from *Synechocystis* sp. PCC 6803. In a $Tyr_D$-less mutant of *Chlamydomonas*, an oxygen-evolving preparation was studied and no evidence for an electrostatic influence was seen (*45*). Thus, some doubts over an electrostatic role exist.

In this work, we present the first single amino acid site-directed mutagenesis in *T. elongatus*. Addition at the same time of a histidine-tag on the C terminus of CP43 allowed the rapid purification of an highly active Y160F−PSII mutant. The enzyme function in the absence of $Tyr_D$ was studied with a range of biophysical methods, and the influences of $Tyr_D$ are defined. In addition, we show that this material can be used to obtain EPR spectra of the active isolated enzyme uncontaminated with $Tyr_D^•$, in particular, some of those originating from the $Mn_4CaO_4$ cluster (e.g., refs *46*−*51*). This genetically engineered strain will thus open the door for future spectroscopic studies.

## EXPERIMENTAL PROCEDURES

*Construction of Mutants.* Two *psbD* genes are present in the genome of *T. elongatus* (*psbD₁* and *psbD₂*)[2] (*11*). The lengths of *psbD₁* and *psbD₂* are both 1056 bp. The amino acid sequences deduced from the nucleotide sequences of these two genes are identical, but *psbD₁* and *psbD₂* differ by four nucleotides. The 3′-terminal region of *psbD₁* overlaps by ≈50 bp with the *psbC* gene, which encodes the CP43 protein. Before doing site-directed mutagenesis in *psbD₁*, deletion of *psbD₂* was done as described below.

*psbD₂* was cloned including the noncoding regions of 800 bp upstream and 780 bp downstream by using PCR amplification (Expand High Fidelity PCR System, Boehringer Mannheim), and the DNA sequences were confirmed. The amplified DNA was subcloned into pUC19 vector. For deletion of *psbD₂* from the wild-type (WT) genome, 910 bp of *psbD₂* between the +150 and +1060 positions, which

[2] Do not mix up *psbD₁*, one of the two genes encoding the D2 protein, with the gene encoding the D1 protein that is *psbA*.

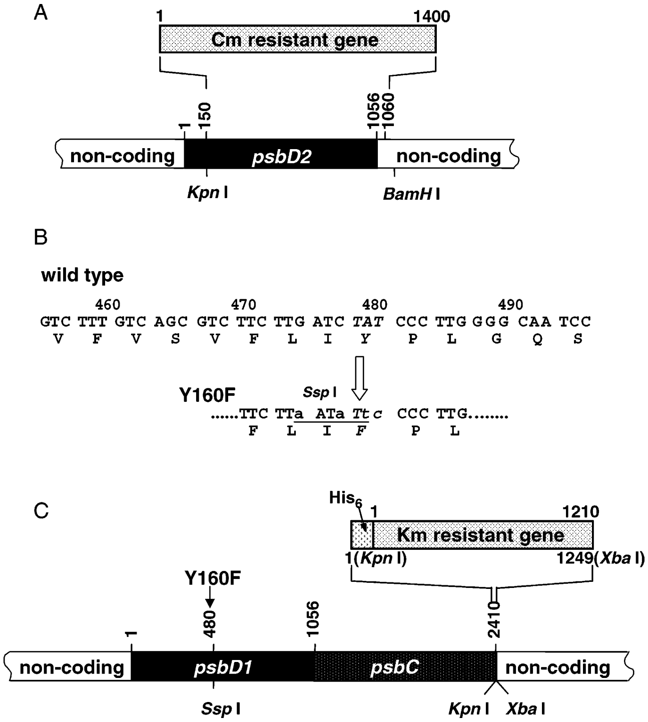


FIGURE 1: Construction of mutants. Knocking out the *psbD*$_2$ gene in *T. elongatus* (A), nucleotide and amino acid sequences around Tyr160 in D2 (B), and Y160F mutation and insertion of a His-tag in *psbD*$_1$/*psbC* genes (C). (A) *psbD*$_2$, showing the 910-bp *Kpn* I/*Bam*H I fragment replaced by a 1.4-kb fragment of a Cm gene cassette resistance. (B) For the Y160F mutation, the TAT (Tyr) codon was replaced by a TTC (Phe) codon. Four nucleotides around the Y160 codon were simultaneously changed for producing an *Ssp* I site without changing the Leu158 and Ile159 amino acids. The substituted nucleotides are shown with small letters, and the *Ssp* I site is underlined. Numbers indicate the nucleotide order from the Met initial codon. (C) *psbD*$_1$, showing the position of the Tyr160 codon. The *Ssp* I site was produced to differentiate the mutant and the WT *psbD*$_1$ in Km$^R$/Cm$^R$-resistant cells (see B). The 1249-bp *Kpn* I/*Xba* I fragment, which has six consecutive His and a Km gene cassette resistance, was inserted just before the stop codon of *psbC*.

includes the stop codon, were replaced by a chloramphenicol (Cm)-resistant gene cassette by using pUD2Cm$^R$3′ as shown in Figure 1A.

*psbD*$_1$ and *psbC* have been previously cloned into the pBluescriptII KS+ vector (*29*). Additional nucleotides encoding six consecutive histidine residues and a kanamycin (Km)-resistant gene cassette were inserted between the 3′ terminus of *psbC* and the noncoding region of *psbC* (pUD243H) (*29*). For the Y160F mutation, the position around +480 in *psbD*$_1$ was modified by using a Quick-Change XL Site-Directed Mutagenesis Kit (Stratagene) and PCR primers as shown in Figure 1B. To have a simple test for the presence of the Y160F mutation and to improve the selection of the mutants, an *Ssp* I restriction site was created together with the codon for Phe160. The construct of the plasmid pUDY160FKm$^R$ is shown in Figure 1C.

*T. elongatus* WT cells were transformed with pUD2Cm$^R$3′ for construction of the *psbD*$_2$-deleted mutant [WT(Δ*psbD*$_2$)], and the recombinant cells were selected by using the Cm antibiotic. For production of the Y160F mutant, the WT-(Δ*psbD*$_2$) cells were transformed with pUDY160FKm$^R$ and selected by DNA analyses prepared from the genome of Km-resistant cells as mentioned below. Transformation was done by electroporation (BioRad gene pulser) with 40 $\mu$L of *T. elongatus* cells (OD$_{730}$ = 60) and 6 $\mu$g of plasmid DNA under the following conditions: 10 kV cm$^{-1}$, 25 $\mu$F, and 200 Ω. After the transformation, cells were spread on a DTN (*29*) plate including 20 $\mu$g of Km mL$^{-1}$ and/or 2.5 $\mu$g of Cm mL$^{-1}$ and cultivated at 45 °C under white fluorescent lamps at ≈30 $\mu$mol of photons m$^{-2}$ s$^{-1}$. Single colonies were streaked onto new DTN plates containing antibiotic(s). To select the mutant cells, the genomic DNA was extracted from the antibiotic-resistant cells, which came from single colonies after the transformation. For confirmation of the segregation on *psbD*$_2$, the region between the upstream and downstream of the *psbD*$_2$ open-reading frame was amplified by PCR, and then its length was analyzed. For the site-directed mutation on *psbD*$_1$, the nucleotides were amplified by using primers, which were designed at positions −35 to −5 and +630 to +660 of *psbD*$_1$. The amplified 695 bp DNA was analyzed with *Ssp* I (New England Biolabs). The single colonies of selected cells were inoculated onto new DTN plates, including 40 $\mu$g mL$^{-1}$ of Km and/or 5 $\mu$g mL$^{-1}$ of Cm. This procedure was repeated until all of the amplified DNA was completely digested into two fragments of 515 and 180 bp. In the following, WT refers to the wild type, WT′ refers to the wild type in which an His-tag has been added to CP43 (*29*), WT(Δ*psbD*$_2$) refers to the wild type in which the *psbD*$_2$ gene has been deleted, Y160F-*psbD*$_1$ refers to the wild type in which the Y160F mutation has been introduced into *psbD*$_1$ by keeping *psbD*$_2$ intact, and Y160F refers to the wild type in which (i) CP43 has a His-tag, (ii) the *psbD*$_2$ gene has been deleted, and (iii) the Y160F mutation has been introduced into *psbD*$_1$.

*Purification of Thylakoids and PSII.* The transformed cells were grown in 1.5 L of DTN with antibiotic(s) in 3-L Erlenmeyer flasks in a rotary shaker with a $CO_2$-enriched atmosphere at 45 °C under continuous light (≈80 $\mu$mol of photons m$^{-2}$ s$^{-1}$). Thylakoids and PSII were prepared as described earlier (*27*, *29*). Routinely, the total amount of Chl before breaking of the cells was 100−150 mg, and the yield after PSII purification in terms of the Chl amount was ≈3%.

*Acetate Treatment.* Untreated isolated Y160F−PSII complexes were diluted to ≈0.1 mg of Chl mL$^{-1}$ in a medium containing 10% glycerol, 0.3 M mannitol, 15 mM $Ca(OH)_2$, 1 M Betaine, and 5 mM 2-(*N*-morpholino)ethanesulfonic acid (Mes) at pH 6.5. Then, the PSII was pelleted by centrifugation (15 min, 170000*g*) after the addition of the same medium containing 50% (w/v) poly(ethylene glycol) (PEG) 8000, so that the final PEG concentration was 15%. Then, the pellet was resuspended in a medium containing 0.5 M acetic acid, 0.3 M mannitol, 15 mM $Ca(OH)_2$, and 40 mM Mes (the pH was adjusted to 5.1 by adding NaOH). PSII was collected by centrifugation (15 min, 170000*g*) after the addition of the same medium containing 50% (w/v) PEG 8000 (the final PEG concentration was 15%). The pellet was resuspended in 0.5 M acetic acid, 0.3 M mannitol, 15 mM $Ca(OH)_2$, and 40 mM Mes at pH 5.1 (with NaOH) and loaded into EPR tubes. After dark adaptation for 1 h at room temperature, 0.5 mM phenyl-*p*-benzoquinone (PPBQ, dissolved in $Me_2$-SO) was added before freezing the sample in liquid $N_2$.

*Oxygen Evolution Measurements.* Oxygen evolution of PSII under continuous light was measured at 25 °C by polarography using a Clark-type oxygen electrode (Hansatech) with saturating white light at a Chl concentration of 2

$\mu$g of Chl $mL^{-1}$ in a medium containing 10 mM NaCl, 15 mM $CaCl_2$, 15 mM $MgCl_2$, 1 M Betaine, and 40 mM Mes at pH 6.5. A total of 0.5 mM DCBQ (2,6-dichloro-*p*-benzoquinone, dissolved in $Me_2SO$) was added as an electron acceptor.

Oxygen evolution under flashing light was measured with a lab-made rate electrode (*27*). Concentration of the thylakoids was 1 mg of Chl $mL^{-1}$ without addition of an electron acceptor. Illumination was done with a xenon flash. The power of the xenon flash was adjusted so that the light intensity was saturating (*27*). Measurements were done at room temperature (20−25 °C). The flash-induced oxygen evolution patterns reported here were obtained as follows: the direct current was recorded with a numerical oscilloscope, and then the derivative versus time was computed mathematically. The derivative step (d $t$) used was d $t$ = 10 ms. The amplitude of the derivative signal $A_n$, which is proportional to the amount of $O_2$ evolved per flash, was plotted versus the flash number. Analysis of the flash-induced oxygen evolution patterns were done using the standard equations listed below assuming that the miss (α) and double-hit ($\beta$) parameters were equal on all flashes

$$[O_2]_n = (1 - \alpha)[S_3]_{n-1} + \beta[S_2]_{n-1} \quad (1)$$

where $[O_2]_n$ is the amount of $O_2$ evolved per PSII reaction center after flash $n$, and $[S_3]_{n-1}$ and $[S_2]_{n-1}$ are the amount of $S_3$ and $S_2$, respectively, before flash $n$

$$[S_i]_n = (1 - \alpha - \beta)[S_{i-1}]_{n-1} + \beta[S_{i-2}]_{n-1} + \alpha[S_i]_{n-1} \quad (2)$$

Because $[O_2]_n$ varies between 0 and 100% and the amount of $O_2$ evolved upon each flash, $A_n$, is an arbitrary value, a scaling factor, $f$, was introduced into the fitting procedure to satisfy the relation $[O_2]_n = fA_n$. The $y$ axis in Figure 3 represents $[O_2]_n$.

*Kinetics of the $S_n$ States in the Dark.* The rate of reduction (or "deactivation"), in the dark, of the $S_3$ and $S_2$ states was determined as follows. Samples, dark-adapted for 1 h on the electrode, were submitted to 2 flashes to form the $S_3$ state in the majority of centers. Then, after a second dark period (the deactivation time), varying from 0.4 s to 60 min, a series of 19 flashes was given. The flash-induced $O_2$ evolution patterns were measured and fitted (using eqs 1 and 2), using the same α and $\beta$ values determined from the flash-induced oxygen evolution pattern (Figure 3), and the $S_3/S_2/S_1/S_0$ contents after each dark time were deduced. For each sample, the concentrations of $S_3$, $S_2$, and $S_1$ versus the dark time after 2 flashes were fitted globally using exponential decays as previously described (ref *27*, also see the Supporting Information).

The oxidation rate in the dark of the $S_0$ state into the $S_1$ state was determined using the following protocol. Samples dark-adapted for 1 h (on the electrode) at room temperature (i.e., mainly in the $S_1$ state) were submitted to 3 flashes to form the $S_0$ state in the majority of centers. Then, after a second dark period, varying from 0.4 s to 60 min, a series of 19 flashes was given. The flash-induced $O_2$ evolution patterns were measured and fitted using eqs 1 and 2 to deduce the $S_3/S_2/S_1/S_0$ concentrations after the varying dark periods. The data were fitted using the following equation:

$$[S_0]_t = ([S_0]_{t=0} - [S_0]_{t=1h}) \exp(-k_4 t) + [S_0]_{t=1h} \quad (3)$$

where $[S_0]_{t=1h}$ is the $S_0$ concentration after 1 h.

*UV−Visible Absorption Changes.* Absorption changes were measured with a lab-built spectrophotometer (*52*), where the absorption changes are sampled at discrete times by short flashes. These flashes were provided by a neodymium:yttriumaluminum garnet (Nd:YAG) pumped (355 nm) optical parametric oscillator, which produces monochromatic flashes (1 nm full-width at half-maximum) with a duration of 6 ns. Excitation was provided by a dye laser pumped by the second harmonic of a Nd:YAG laser (685 nm, 1 mJ). PSII was used at 25 $\mu$g of Chl $mL^{-1}$ in 15 mM $CaCl_2$, 15 mM $MgCl_2$, 1 M Betaine, and 40 mM Mes at pH 6.5. After dark adaptation for 1 h at room temperature (20−22 °C), 0.1 mM PPBQ was added as an electron acceptor.

*Fitting of the Flash-Induced Absorption Changes at 292 nm.* For technical reasons, the analytic laser flash had a small actinic effect. To partially take into account this effect, the data were fitted using a double-hit parameter different from zero. First, the two parameters, α (miss) and $\beta$ (double hit), were calculated by using the procedure developed by Lavorel (*53*). Then, the 3 differential extinction coefficients, $\Delta\epsilon_0$, $\Delta\epsilon_1$, and $\Delta\epsilon_2$ (corresponding to the $S_0 \rightarrow S_1$, $S_1 \rightarrow S_2$, and $S_2 \rightarrow S_3$ transitions, respectively) were estimated by using the fitting procedure developed by Lavergne (refs *54* and *55*, also see the Supporting Information).

*Time-Resolved Absorption at 820 nm.* Excitation flashes (300 ps, 532 nm) were provided with a Nd:YAG laser (Quantel, Les Ulis, France) at a repetition rate of 1 Hz. The flash energy at the sample was varied between ∼4 mJ $cm^{-2}$ and ∼250 $\mu$J $cm^{-2}$ by insertion of neutral density filters. Such variation was found to change only the amplitude of the absorption changes, while the kinetics were superimposable within the signal−noise ratio after normalization of the amplitudes. The measuring light was provided by a continuous wave (cw) laser diode emitting at 820 nm (SDL-5411-G1, Spectra Diode Labs, San Jose, CA). A cutoff filter RG780 was placed before the cuvette and an 820-nm interference filter (10-nm bandwidth), after the cuvette (path length = 10 mm, 2 mm broad). The measuring light intensity and the flash-induced changes were monitored behind the sample, and the interference filter with a photodiode (FND 100, EG and G, Salem, MA) was connected to an amplifier (HCA, 28 dB, DC-325 MHz; FEMTO, Berlin, Germany) and a digital storage oscilloscope DSA 602A with plug-in 11A52 (DC-100 MHz, Tektronix, Beaverton, OR). Typically, 16 signals were averaged to improve the signal-to-noise ratio. The kinetic data were fitted into a multiexponential decay with a Marquart least-squares algorithm program kindly provided by P. Setif (CEA Saclay). Time zero was set at half-rise of the absorption increase. Fitting was started 10 ns after time zero to exclude a very fast phase with a $t_{1/2} \leq$ 3 ns that might be due to the decay of singlet excited Chls. Relative amplitudes of the exponential phases are quoted for time zero. Samples were in a medium containing 10 mM NaCl, 15 mM $CaCl_2$, 15 mM $MgCl_2$, 1 M Betaine, and 40 mM Mes at pH 6.5, with 0.5 mM PPBQ as an electron acceptor.

*EPR Spectroscopy.* cw-EPR spectra were recorded using a standard ER 4102 (Bruker) X-band resonator with a Bruker ESP300 X-band spectrometer equipped with an Oxford Instruments cryostat (ESR 900). Flash illumination at room temperature was provided by a Nd:YAG laser (532 nm, 550 mJ, 8 ns Spectra Physics GCR-230-10). PSII samples at ≈1 mg of Chl $mL^{-1}$ were loaded in the dark into quartz EPR tubes and further dark-adapted for 1 h at room temperature. Then, the samples were synchronized in the $S_1$ state with one preflash (*40*). After another dark period of 1 h at room temperature, 0.5 mM PPBQ dissolved in $Me_2SO$ was added (the final concentration of $Me_2SO$ was ≈2%). After illumination by the indicated number of flashes, the samples were frozen in the dark to 198 K, degassed at 198 K as already described (*21*), and then transferred to 77 K. Near-infrared illumination of the samples was done directly in the EPR cavity and was provided by a laser diode emitting at 820 nm (Coherent, diode S-81-1000C) with a power of 600−700 mW at the level of the sample (*56*).

*Fourier Transform Infrared (FTIR) Measurements.* For the measurements of $P_{680}{}^{+}/P_{680}$ FTIR difference spectra, PSII was depleted of Mn by an $NH_2OH$ (10 mM) treatment for 1 h at room temperature in a 10 mM Mes-NaOH buffer (pH 6.0) containing 50 mM sucrose, 10 mM NaCl, 0.5 mM EDTA, and 0.06% *n*-dodecyl-*β*-maltoside (*β*DM). The PSII was then washed using the same buffer and concentrated to about 6 mg of Chl $mL^{-1}$, using a Microcon-100 (Amicon). The sample (5 μL) was mixed with 0.5 μL of 1 M potassium ferricyanide and 0.5 μL of 20 mM silicomolybdate, lightly dried on a $BaF_2$ plate under $N_2$ gas flow, and covered with another $BaF_2$ plate with 1 μL of water. The sample temperature was adjusted to 265 K in a liquid $N_2$ cryostat (Oxford DN1704) using a controller (Oxford ITC-5). FTIR spectra were recorded on a Bruker IFS-66/S spectrophotometer equipped with an MCT detector (Infrared D316/8). The $P_{680}{}^{+}/P_{680}$ spectrum was obtained as a difference between the measurements in the dark for 1 s and during illumination for 1 s. This dark−light cycle was repeated 1000 times, and the spectra were averaged. The final data were obtained as an average of the spectra recorded using two different samples. Illumination was performed with continuous white light from a halogen lamp (Hoya-Schott HL150) with a light intensity of about 60 mW $cm^2$ at the sample surface. The spectral resolution was 4 $cm^{-1}$.

## RESULTS

*Expression of the psbD₂ Gene and Construction of the Y160F Mutant.* Two *psbD* genes are present in the genome of *T. elongatus* (*psbD₁* and *psbD₂*) (*11*). Because the relative level of expression of these genes was not known in this organism, in the early stages of this work, the Y160F mutation in the D2 protein was done by changing the TAT (Tyr) codon into the TTC (Phe) codon in *psbD₁* without knocking out the *psbD₂* gene (Figure 1). To confirm that all copies of the *psbD₂* genes were completely segregated, single colonies of the Y160F-*psbD₁* mutant cultivated on plates were grown in a liquid culture under a light intensity of ≈60 μmol of photons $m^{-2}$ $s^{-1}$. The $Tyr_D$ content in the Y160F-*psbD₁* mutant cells was estimated and compared to that in the WT′ cells, cultivated under the same conditions, by measuring the $Tyr_D{}^{\bullet}$ EPR signal (Figure 2). The amplitude of the $Tyr_D{}^{\bullet}$ EPR signal in different batches of cells was

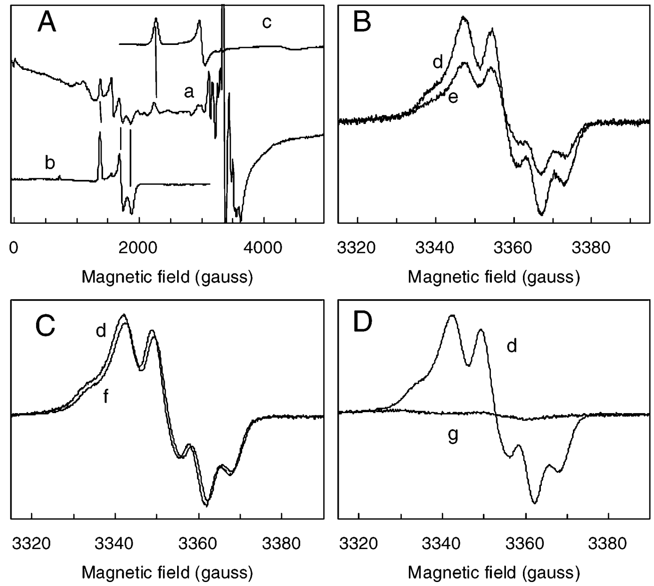


FIGURE 2: EPR spectra recorded on whole cells. (A) Spectrum a, EPR spectrum recorded on WT′ whole cells. Spectrum b, EPR spectrum of purified FeSOD from *T. elongatus* (*57*). Spectrum c, EPR spectrum of purified cytochrome *c*550 from *T. elongatus* (*68*). The vertical lines indicate the resonances used for quantification. (B−D) Spectra d, $Tyr_D{}^{\bullet}$ EPR signal recorded in WT′ cells. (B) Spectrum e, $Tyr_D{}^{\bullet}$ EPR signal recorded in Y160F-*psbD₁* cells. (C) Spectrum f, $Tyr_D{}^{\bullet}$ EPR signal recorded in WT(Δ*psbD₂*) cells. (D) Spectrum g, $Tyr_D{}^{\bullet}$ EPR signal recorded in Y160F cells. For A, the instrument settings were temperature = 15 K, modulation amplitude = 25 G, microwave power = 20 mW, microwave frequency = 9.4 GHz, and modulation frequency = 100 kHz. For B−D, the instrument settings were temperature = 15 K, modulation amplitude = 2.8 G, microwave power = 2 μW, microwave frequency = 9.4 GHz, and modulation frequency = 100 kHz.

calibrated as follows. The EPR spectra of whole cells were recorded (spectrum a of Figure 2A), and the relative concentration of the different batches of cells was estimated by using two internal EPR probes: (i) the three major resonances of the high-spin $S = {}^{5}/_{2}$ $Fe^{III}$ signal originating from superoxide dismutase (FeSOD) (spectrum b of Figure 2A) (*57*) and (ii) the $g_z$ resonance of the unbound cytochrome *c*550 signal (spectrum c of Figure 2A) (*58*). The PSII-bound cytochrome *c*550 seems to be undetectable under these experimental conditions. In the course of this study, it was found that the ratio of FeSOD to unbound cytochrome *c*550 was almost constant so that either of these proteins could be considered as being proportional to the cell concentration. In addition, the concentration of these two proteins inside the cells relative to PSII (measured as $Tyr_D{}^{\bullet}$) was not significantly affected by the different mutations made here (results not shown). Additional features can be seen in Figure 2A: (i) signals at ≈1000 and 1600 G from unidentified $Fe^{III}$, (ii) the 6 lines from $Mn^{II}$ between 3000 and 4000 G (similar amounts of $Mn^{II}$ were found in the WT and mutants cells), and (iii) the narrow $Tyr_D{}^{\bullet}$ signal at ≈3350 G, which is out of scale under these recording conditions.

Figure 2B compares the amplitude of the $Tyr_D{}^{\bullet}$ EPR signal in the WT′ cells (spectrum d) to that in the Y160F-*psbD₁* cells (spectrum e). The amplitude of the $Tyr_D{}^{\bullet}$ EPR signal in the Y160F-*psbD₁* cells was ≈50% of that in the WT′ cells. Analysis of *psbD₁* in these Y160F-*psbD₁* cells showed that the *Ssp* I restriction site introduced together with the Y160F mutation was retained. These results suggest that under these conditions the *psbD$_2$* gene is expressed.

Therefore, before introducing the Y160F mutation in the *psbD$_1$* gene, the *psbD$_2$* gene was deleted from the chromosome and replaced by a Cm-resistant gene cassette, WT-($\Delta$*psbD$_2$*), (Figure 1). Figure 2C shows that the $Tyr_D^{\bullet}$ content in the WT($\Delta$*psbD$_2$*) cells (spectrum f) was similar to that in the WT′ cells (spectrum d), showing that the PSII content was not affected by the deletion of *psbD$_2$*. The option of knocking out *psbD$_1$* and introducing the mutation into *psbD$_2$* was not chosen because complications may arise from the overlap between *psbC* and *psbD$_1$* (Figure 1). When the Y160F-*psbD$_1$* mutation was introduced into the WT($\Delta$*psbD$_2$*) as the host cells (together with the addition of the His-tag on CP43 encoded by *psbC*), the resulting cells completely lacked the $Tyr_D^{\bullet}$ EPR signal (spectrum g of Figure 2D).

Two copies of the *psbD* gene are also encountered in *Synechocystis* sp. PCC 6803 and *Synechococcus* sp. PCC 7942. Although the relative level of expression of the *psbD$_1$* and *psbD$_2$* genes is not clear, it has been shown that *psbD$_1$* is constitutively expressed in *Synechococcus* sp. PCC 7942, whereas the transcription of *psbD$_2$* occurs under high light (350 $\mu$mol of photons $m^{-2}$ $s^{-1}$) (*59*). In *Synechocystis* sp. PCC 6803, it seems that only *psbD$_1$* is constitutively expressed and that *psbD$_2$* is not expressed (M. Ikeuchi, personal communication). In earlier work on *Synechocystis* sp. PCC 6803, to avoid potential problems, *psbD$_2$* was deleted before introducing the Y160F mutation in *psbD$_1$* (*30*, *31*).

It is worth noting that, before we produced the *psbD$_2$*-deleted strain, a strain was made in which the *psbD$_2$* gene was inactivated by insertion of a spectinomycin/streptomycin-resistant cassette and the Y160F mutation in *psbD$_1$* (together with the addition of the His-tag on *psbC*) was introduced. Despite confirmation of complete segregation of the genome in single colonies after cultivation on plates, during continuous cultivation in liquid, we observed that (i) the *Ssp* I sequence was lost and *psbD$_1$* reverted to the WT sequence and/or (ii) the *psbD$_2$* gene recovered its normal length even though the resistance to spectinomycin/streptomycin was retained. These results indicate the occurrence of recombination processes between *psbD$_2$* and *psbD$_1$* and the displacement of the antibiotic resistance cassette within the genome.

The growth rate of the different strains was measured either under moderate light intensity ($\approx$60 $\mu$mol of photons $m^{-2}$ $s^{-1}$) or low light intensity ($\approx$15 $\mu$mol of photons $m^{-2}$ $s^{-1}$) (see the Supporting Information). When the cells were cultivated under the moderate light intensity, the doubling times of the WT′, WT($\Delta$*psbD$_2$*), and Y160F cells were approximately 16, 16, and 25 h, respectively. Under low light intensity, the doubling times were approximately 33, 32, and 39 h, respectively. Also detectable was a marked lag in the growth of Y160F cells, which is absent in the WT′ and WT($\Delta$*psbD$_2$*) cells (see the Supporting Information).

*Oxygen Evolution.* The oxygen evolution activities of purified WT′−PSII and Y160F−PSII measured under continuous saturating light were found to be similar and close to 3500 $\mu$mol of $O_2$ $mg^{-1}$ of Chl $h^{-1}$ using DCBQ as an electron acceptor at 25 °C and pH 6.5.

*Flash-Induced Oxygen Evolution and S-States Deactivation.* Flash-induced $O_2$ evolution patterns from WT′ and Y160F thylakoids dark-adapted for 1 h at room temperature on the polarized electrode are shown in Figure 3. This technique requires the use of thylakoids (or cells) rather than isolated PSII because sedimentation of the sample on the bare platinum electrode is required. From the fit of the sequences (eqs 1 and 2 in the Experimental Procedures), the following parameters were obtained: in WT′, $\alpha = 8\%$, $\beta = 7\%$, $S_1 = 85\%$, and $S_0 = 15\%$ (···, Figure 3); in Y160F, $\alpha = 9\%$, $\beta = 6\%$, $S_1 = 72\%$, and $S_0 = 28\%$ (—, Figure 3). The $\alpha$ and $\beta$ parameters were found to be similar in both samples. By contrast, the proportion of $S_0$ was significantly higher in Y160F thylakoids. As expected, the absence of $Tyr_D^{\bullet}$ eliminated the conversion of $S_0$ into $S_1$ in the dark, which normally occurs via the $S_0Tyr_D^{\bullet} \rightarrow S_1Tyr_D$ reaction (*40*).

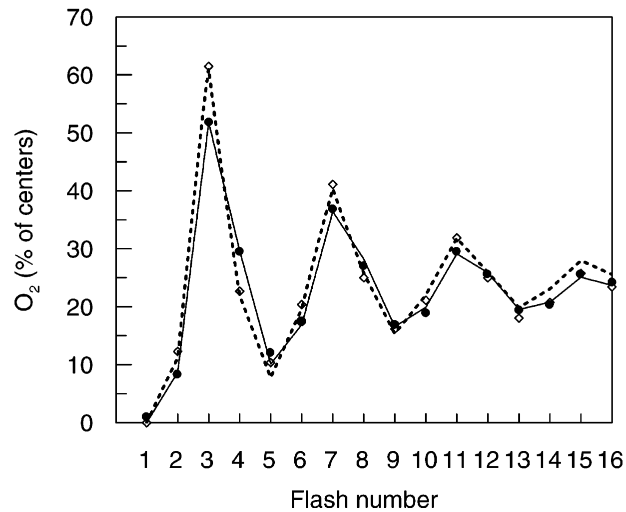


FIGURE 3: Flash-induced oxygen evolution patterns. Data were recorded during a sequence of saturating xenon flashes (spaced 400 ms apart) with WT′ thylakoids (◇) and Y160F thylakoids (●). The samples (Chl = 1 mg $mL^{-1}$) were dark-adapted for 1 h at room temperature on the polarized bare platinum electrode. Amplitude of the flash-induced oxygen evolution has been plotted so that it corresponds directly to the percentage of centers in which $O_2$ is produced as explained in the Experimental Procedures. The continuous and dashed lines are the results of the fitting procedure for the Y160F and WT′ thylakoid samples, respectively. The $S_1/S_0$ ratio and $\alpha$ and $\beta$ parameters used for the fits are given in the Results.

The stability of the $S_n$ states in the Y160F enzyme was investigated by using a Joliot-type $O_2$ electrode. The plots of the $S_3/S_2/S_1$ concentrations versus the dark time in WT′ and Y160F thylakoids are shown in parts A and B of Figure 4, respectively. Results from the fits are listed in Table 1.

In WT′ thylakoids, the $S_3$, $S_2$, and $S_1$ concentrations were free parameters in the fitting procedure. The $S_3$−$S_2$ deactivation was found to be biphasic, and the three fitted curves satisfactorily follow the $S_3$, $S_2$, and $S_1$ concentrations measured experimentally (Table 1). In the Y160F thylakoids, the experimental data points are qualitatively different: (i) decay of $S_3$ was well-fitted using a single exponential, and (ii) the formation of $S_1$ did not correspond to the sum of the decay of $S_3$ and $S_2$. The best fit of the data in Figure 4B was obtained by using only $S_3$ and $S_2$ concentrations as the free parameters. While the fits are satisfactory for the $S_3$ and $S_2$ concentrations, for the longer dark periods, the calculated curve for the $S_1$ concentrations deviated significantly from the experimental data (Figure 4B). This suggests that in Y160F thylakoids the kinetic model was not fully appropri-

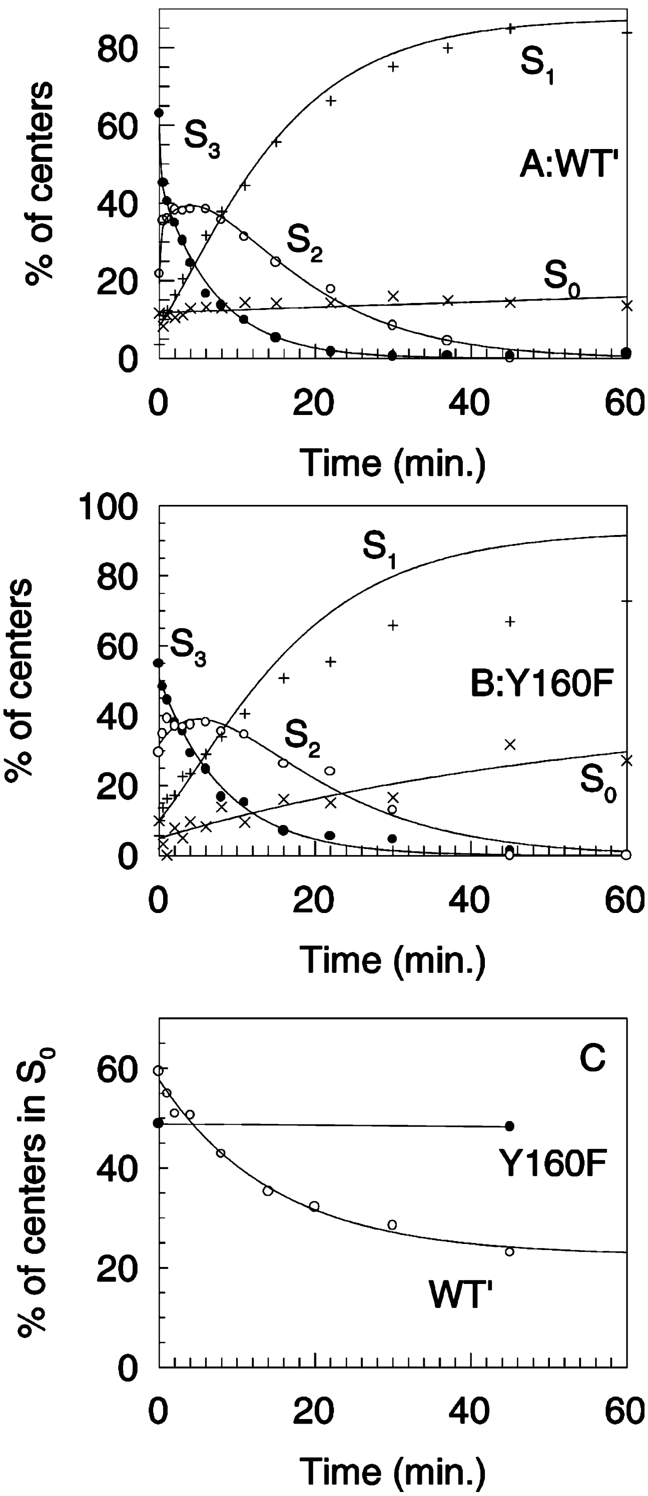


FIGURE 4: Deactivation kinetics. Deactivation of the $S_3$ and $S_2$ states and formation of the $S_1$ and $S_0$ states after 2 saturating flashes, at room temperature, in WT′ thylakoids (A) and Y160F thylakoids (B). (C) Kinetics of the $S_0$−$S_1$ state conversion after 3 saturating flashes in WT′ thylakoids (○) and Y160F thylakoids (●). See the Experimental Procedures for other details.

ate. This is further supported by the time dependence in the dark of the $S_0$ concentration. While in WT′ thylakoids, the $S_0$ concentration was found almost constant during the dark periods (×, Figure 4A), in Y160F thylakoids, the $S_0$ concentration increased slowly in the dark (×, Figure 4B) probably to the detriment of $S_1$. This would explain the overestimate of $S_1$ in the fitted curve. In Y160F thylakoids, after the 2 preflashes, the $S_0$ level was ≈8% and increased with a $t_{1/2}$ of approximately 30 min to reach ≈30% after 60 min. Such results show that, under conditions in which the Y160F thylakoids were sedimented onto a polarized electrode, there is probably a slow reduction of $S_1$ in ≈30% of the centers.

Table 1: Deactivation Kinetics for $S_3$, $S_2$, and $S_0$[a]

| | $S_3 \rightarrow S_2$ | | $S_2 \rightarrow S_1$ | | $S_0 \rightarrow S_1$ | |
|---|---|---|---|---|---|---|
| | % | $t_{1/2}$ | % | $t_{1/2}$ | % | $t_{1/2}$ |
| WT′ thylakoids | 76 | 4.9 min | 100 | 7.5 min | 62 | 9.9 min |
| | 24 | 7.8 s | | | 38 | constant |
| Y160F thylakoids | 100 | 5.8 min | 100 | 8.2 min | | not observed |

[a] Deactivation kinetics of the $S_3$ state into the $S_2$ state and the $S_2$ state into the $S_1$ state and kinetics of oxidation in the dark of the $S_0$ state into the $S_1$ state in WT′ and Y160F thylakoids.

For the short dark periods, where the kinetic model is not complicated by the apparent slow decay of $S_1$, results in Figure 4 show that the fast phase with a $t_{1/2}$ of 7.8 s, observed for the $S_3$ reduction in WT′ thylakoids, was absent in Y160F thylakoids. This confirms the suggestion made earlier (*27*) that the $t_{1/2}$ of 7.8 s in WT′ thylakoids corresponds to the reduction of $S_3$ into $S_2$ by $Tyr_D$. The slow phase for the $S_3$ reduction into $S_2$ in WT′ thylakoids was found to be similar to the main phase in Y160F thylakoids. The rate of $S_2$ reduction into $S_1$ was found to be close in the WT′ and Y160F thylakoids.

The oxidation rate in the dark of the $S_0$ state into the $S_1$ state in samples prepared to contain a high amount of $S_0$ are shown in Figure 4C for WT′ and Y160F thylakoids. The data were fitted using eq 6 in the Experimental Procedures. In WT′ thylakoids, the disappearance of the $S_0$ state occurred with a $t_{1/2}$ of ≈ 10 min for 62% of the initial $S_0$ concentration. The remaining 38% of the initial $S_0$ concentration was longer-lived than the time scale used here. In Y160F thylakoids, the $S_0$ state was stable in the experimental time range. These results clearly confirm that the oxidation in the dark from $S_0$ to $S_1$ (*60*) results from the $S_0Tyr_D^{\bullet}$ to the $S_1Tyr_D$ reaction (*40*).

The rate of oxygen release on the $S_3Tyr_Z^{\bullet} \rightarrow S_0Tyr_Z$ transition can be roughly estimated with the electrode used above (*27*, *61*). The $t_{1/2}$ for the oxygen release was estimated to be 1−2 ms both in WT′ and Y160F thylakoids (see the Supporting Information). This confirms that the mutation had no effect on the limiting step in the oxygen evolution process.

*$P_{680}^+$ Reduction Kinetics.* Flash-induced absorption changes at 820 nm were measured with a time resolution of about 3 ns on WT′−PSII and Y160F−PSII (see the Supporting Information). The Y160F mutation had small but reproducible effects on $P_{680}^+$ reduction, namely, a slight acceleration in the tens of nanoseconds scale and some slowing in a scale from a few microseconds to a few hundreds of microseconds. Five exponentials were required for acceptable fits in the range from 10 ns to 1.6 ms. With more than five exponentials, the best-fit parameters varied considerably between independent experiments on the same type of sample. The best-fit parameters with five exponentials were for WT′, $t_{1/2}$ (a) = 19 ns (28% of the total decay), $t_{1/2}$ (b) = 92 ns (19%), $t_{1/2}$ (c) = 2 $\mu$s (19%), $t_{1/2}$ (d) = 35 $\mu$s (23%), and $t_{1/2}$ (e) = 211 $\mu$s (11%); and for Y160F, $t_{1/2}$ (a) = 16 ns (30%), $t_{1/2}$ (b) = 70 ns (22%), $t_{1/2}$ (c) = 3 $\mu$s (12%), $t_{1/2}$ (d) = 49 $\mu$s

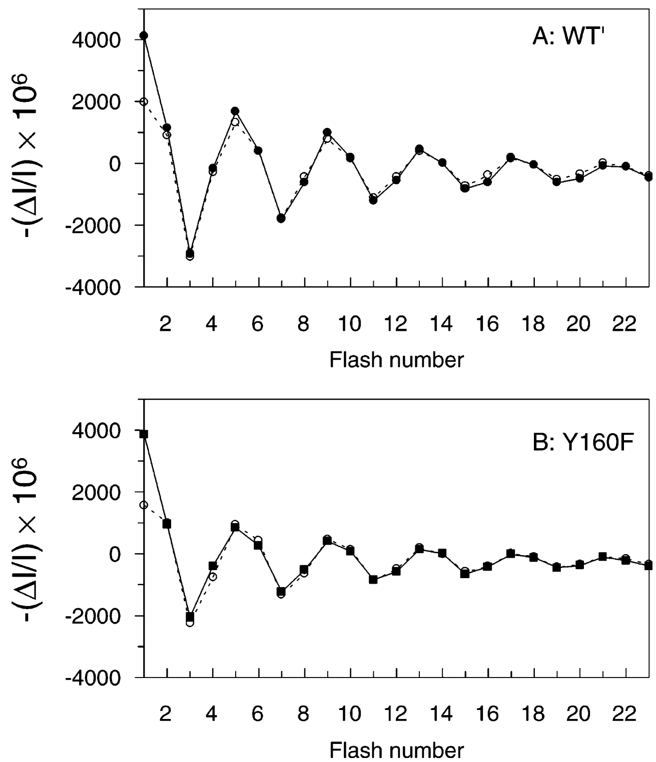


FIGURE 5: Sequence of the amplitude of the absorption changes at 292 nm. Measurements were done during a series of saturating flashes (spaced 400 ms apart) given on WT′−PSII (●, A) and Y160F−PSII (■, B). The samples (Chl = 25 $\mu$g mL$^{-1}$) were dark-adapted for 1 h at room temperature before the addition of 100 $\mu$M PPBQ (dissolved in $Me_2SO$). The measurements were done 300 ms after each flash. Open symbols and dotted lines correspond to fitted data calculated as described in the Results.

(25%), and $t_{1/2}$ (e) = 316 $\mu$s (11%). The qualitative mutation effects described above are reflected in the fit parameters mainly by slightly shorter $t_{1/2}$ values and larger relative amplitudes of the two fastest phases a and b, a longer $t_{1/2}$ and smaller amplitude of phase c, and a longer $t_{1/2}$ of the slowest phase e.

We consider these fits as the simplest acceptable mathematical description of our experimental data, rather than as a true representation of all kinetic processes involved in the reduction of $P_{680}{}^+$. Because $P_{680}{}^+$ reduction is known to depend on the S states and to be already multiphasic in each S state (*37*−*39*), more than five kinetic phases are likely to contribute under repetitive excitation conditions. An improved signal-to-noise ratio would be required to resolve a larger number of kinetic phases. Nevertheless, our data provide a global view of the effect of the absence of $Tyr_D{}^•$ on the reduction kinetics of $P_{680}{}^+$.

*Flash-Induced Absorption Changes at 292 nm.* The amplitude of the absorption changes upon flash illumination was measured in the hundreds of milliseconds time range (i.e., after the reduction of $Tyr_Z{}^•$ by the $Mn_4CaO_4$ complex was complete) using a Joliot-type spectrophotometer (*39*, *52*, *55*) at 292 nm. This wavelength corresponds to an isobestic point for $PPBQ^-$/PPBQ (not shown) and is in a spectral region where the absorption of the $Mn_4CaO_4$ complex depends on the S states (*55*).

Figure 5 shows the oscillation pattern in the absorption amplitude at 292 nm (● and ■, —) observed with WT′−PSII (A) and Y160F−PSII (B). Period four oscillations are clearly visible at least until the 23rd flash. Using the formula developed by Lavorel (*53*) and the oscillating patterns in Figure 5, the following values were obtained: in WT′−PSII, $\alpha$ = 6% and $\beta$ = 5%; and in Y160F−PSII, $\alpha$ = 7% and $\beta$ = 6%. The miss parameters are close to those obtained in Figure 3 for the flash-induced oxygen evolution patterns, and they show that the Y160F mutation has also little effect on the oscillating properties in purified PSII. In this experiment, the double-hit parameter does not depend on the PSII properties and cannot be compared to those determined in Figure 3 (see the Experimental Procedures).

Data in Figure 5 were fitted as described in the Experimental Procedures (○, Figure 5). The first data point was not included into the fit as discussed earlier (*55*). In dark-adapted WT′−PSII, we obtained 100% $S_1$ and in dark-adapted Y160F−PSII we obtained 79% $S_1$ and 21% $S_0$. These percentages are close to those deduced from the fits of the flash-induced oxygen evolution patterns (Figure 3). The $\Delta\epsilon_0$, $\Delta\epsilon_1$, and $\Delta\epsilon_2$ corresponding to the $S_0$−$S_1$, $S_1$−$S_2$, and $S_2$−$S_3$ transitions, respectively, found here were 0.20 × $10^{-3}$, 2.26 × $10^{-3}$, and 1.24 × $10^{-3}$, respectively. These values are remarkably close to those found earlier at 292 nm in PSII from plants[3] (*55*).

*Flash-Induced Absorption Changes around 430 nm.* Figure 6 shows the absorption changes from 415 to 450 nm in WT′−PSII (A) and Y160F−PSII (B) after the first 6 flashes of a series. Measurements were done 5 ns after the flashes. In this spectral region, the redox changes of several species, such as the Chls , cytochromes, and $Tyr_Z$, give rise to absorption changes. The largest absorption change however is expected to reflect the formation of $P_{680}{}^+$ upon light-induced oxidation. It gives rise to a strong bleaching in the 430 nm region. In WT′−PSII (A), the spectra observed after each flash in a series were slightly but significantly different. After the second flash (●), i.e., in the $S_2P_{680}{}^+$ state, the spectrum was slightly red-shifted when compared to the spectrum after the first flash, i.e., in the $S_1P_{680}{}^+$ state (○). Figure 6C shows a plot of the absorption changes measured at 439 nm in WT′−PSII (●) upon each flash of a sequence. A clear period four oscillation is observed. Similar oscillations occurred at all wavelengths above 433 nm, and below 433 nm, the oscillating pattern was inverted. In Y160F−PSII, the spectra differ slightly from those in WT′−PSII (B) and variations of the spectra depending on the flash number were less-marked in Y160F−PSII (■, Figure 6C) than in WT′−PSII (● in Figure 6C).

Several nonexclusive hypotheses may account for this dependence upon the S states of the absorption changes observed shortly after the flash: (i) it may reflect the $S_n$-state-dependent $P_{680}{}^+$ reduction rate, (ii) $P_{680}$ or other Chls in the PSII complex may undergo an electrochromic shift upon the $S_n$-state turnover, or (iii) a change may occur in the relative contribution from the various Chls (such as $P_{D1}$

[3] Values of the extinction coefficients correspond to samples with a Chl concentration of 25 $\mu$g mL$^{-1}$ with 43 Chls per PSII reaction (*27*) and a path length of the sample of 2.5 mm. In the previous work on PSII from plants (*55*), values of the extinction coefficients corresponded to samples with ≈220 Chls per PSII reaction center, the Chl concentration was 12.5 $\mu$g mL$^{-1}$, and the path length of the sample was 15 mm.

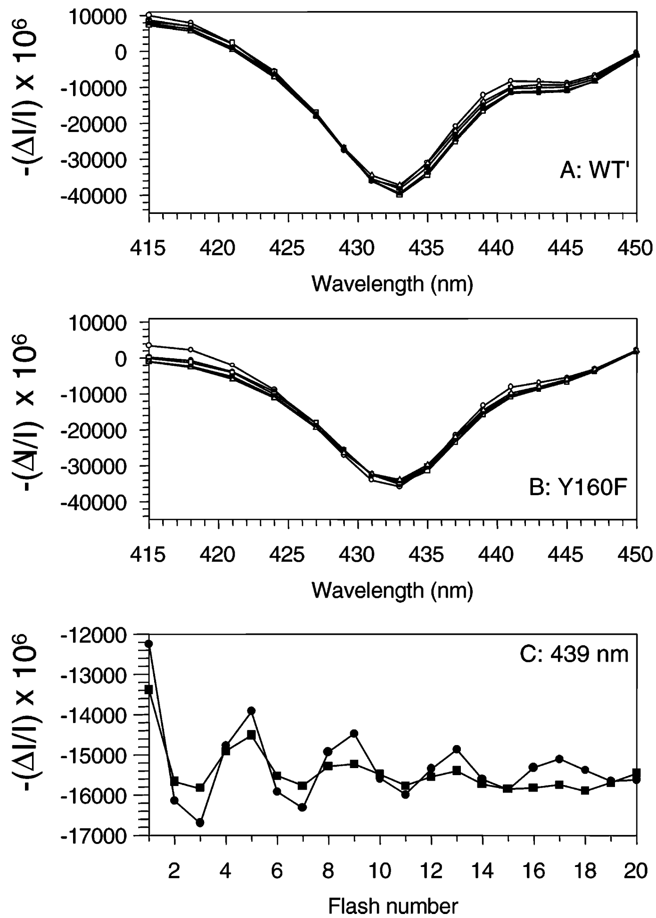


FIGURE 6: Difference spectra around 430 nm. In A (for WT′−PSII) and B (for Y160F−PSII), flash-induced absorption changes were measured 5 ns after each flash (spaced 400 ms apart) of a sequence: 1st flash (○), 2nd flash (●), 3rd flash (□), 4th flash (■), 5th flash (△), and 6th flash (▲). (C) Sequence of the amplitude of the absorption changes at 445 nm measured 10 ns after each flash of a series in WT′−PSII (■) and Y160F−PSII (●). Other conditions are the same as in Figure 5.

and $P_{D2}$) undergoing absorbance changes upon $P_{680}^+$ formation. Discriminating between the two latter hypothesis is difficult; however, the first hypothesis is unlikely to account solely for the oscillating pattern because, in this case, one would observe homothetic spectra upon each flash in a series and this is not seen in data shown in parts A and B of Figure 6.

Irrespective of the origin of the oscillating spectral contribution, the data for WT′−PSII in Figure 6C can be fitted with the same protocol as that used in Figure 5 and by using the miss and double-hit parameters and the $S_1/S_0$ ratio used to fit the flash-induced absorption changes at 292 nm (see the Supporting Information). This fitting procedure results in 3 extinction coefficients $\Delta\epsilon_0$, $\Delta\epsilon_1$, and $\Delta\epsilon_2$ corresponding to the absorption changes upon formation of the $S_1P_{680}^+$, $S_2P_{680}^+$, and $S_3P_{680}^+$ transitions, respectively. This allows us to simulate a theoretical flash sequence by keeping constant the 3 extinction coefficients $\Delta\epsilon_0$, $\Delta\epsilon_1$, and $\Delta\epsilon_2$ and by varying the $S_1/S_0$ ratio from 1:0 to 0.7:0.3, i.e., values close to those found in WT′−PSII and Y160F−PSII, respectively. The result of such a procedure clearly showed that the weaker oscillations in Y160F−PSII could not be explained only by a higher proportion of $S_0$ in the dark-adapted material (see the Supporting Information). Consequently, the $\Delta\epsilon_0$, $\Delta\epsilon_1$, and $\Delta\epsilon_2$ in Y160F−PSII must also differ from those in WT′−PSII, as expected, because the spectra differ in A and B of Figure 6.

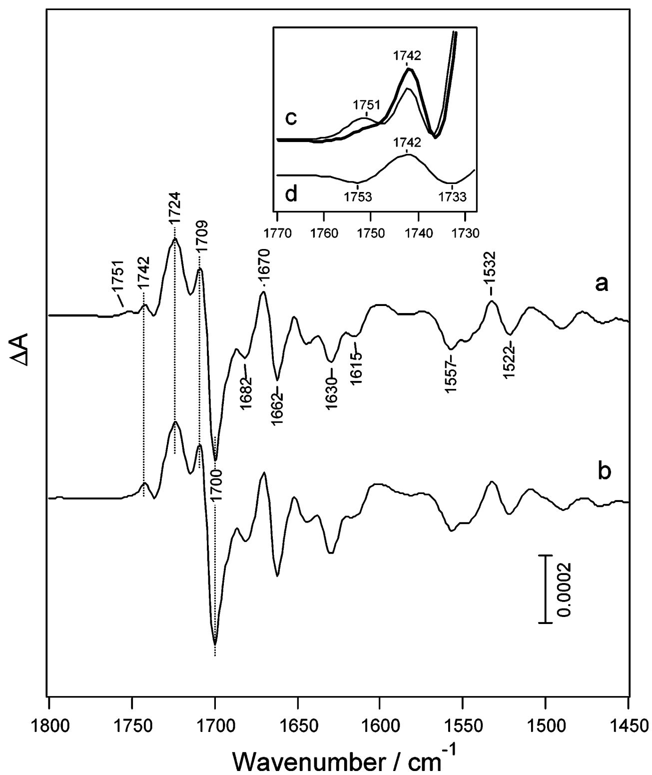


FIGURE 7: $P_{680}^+/P_{680}$ FTIR difference spectra. Measurements were done in WT′−PSII (a) and Y160F−PSII (b) at 265 K. Inset, (c) expanded spectra in the 1770−1730 cm$^{-1}$ region for WT′−PSII (thin line) and Y160F−PSII (thick line), and (d) double difference spectrum as Y160F minus WT′.

From the data in Figure 6A, it also appears that the flash-induced spectral changes were more pronounced above 433 nm than below this wavelength. This could occur if the $P_{D2}$ spectrum, in addition to being red-shifted, is also slightly broader than the $P_{D1}$ spectrum. Such a broadening could indicate a slightly different electronic coupling between $P_{D1}$ and $P_{D2}$ in the $P_{D1}P_{D2}^+$ states in Y160F−PSII.

*FTIR Spectra of $P_{680}^+/P_{680}$.* Figure 7 shows the $P_{680}^+/P_{680}$ difference spectra in Mn-depleted WT′−PSII (spectrum a) and Y160F−PSII (spectrum b). The overall features were basically similar. In particular, the frequencies and intensities of the negative peak at 1700 cm$^{-1}$ and the positive peaks at 1724 and 1709 cm$^{-1}$ were virtually unchanged. These bands were attributed to the keto C=O stretching bands of $P_{680}$ (negative peak at 1700 cm$^{-1}$ and positive peaks at 1724 and 1709 cm$^{-1}$) (*62*−*64*). This indicates that the charge distribution and basic structure of $P_{680}$ did not drastically change in Y160F−PSII. Nevertheless, one clear change was observed in the small positive peaks at 1751 and 1742 cm$^{-1}$ (inset c of Figure 7). The 1751 cm$^{-1}$ peak diminished, and the intensity of the 1741 cm$^{-1}$ peak increased in Y160F−PSII. The double difference spectrum in this region (inset d of Figure 7) showed a (−/+/−) peak pattern at 1753/1742/1733 cm$^{-1}$ with the positive 1742 cm$^{-1}$ peak being strongest, suggesting that the possible differential signal at 1751(+)/∼1742(−) cm$^{-1}$ downshifted by about 10 cm$^{-1}$ in Y160F−PSII. It is noted that this signal change was reproducibly observed with different batches of the sample (although we cannot completely eliminate the possibility that these changes occur upon the Mn depletion procedure, the robustness of the Y160F−PSII seems to argue against this hypothesis). These peaks have been attributed either to the carbomethoxy C═O stretch of a Chl molecule (*65*) or to the C═O stretch of a protonated carboxylic acid of the protein (*66*). The former assignment seems more likely because no carboxylic acid residues are found within 10 Å around both $Tyr_D$ and $P_{680}$ in the X-ray crystal structure (*7*). We cannot completely eliminate the possibility.

*EPR Spectroscopy.* Figure 8 shows the EPR spectra recorded at 9 K on Y160F−PSII. Spectrum a was recorded on a sample in the $S_1$ state, and spectrum b was recorded after the sample was illuminated by one flash at room temperature, i.e., in the $S_2$ state. Spectrum b exhibits the $S_2$-multiline signal. The additional features that can be seen in the spectrum (Figure 8A) are as follows: (i) the $g_z$ and $g_y$ resonances of cytochrome *c*550 at ≈2230 and ≈2920 G, respectively (*60*), (ii) a signal at $g = 4.3$ (≈1600 G) from a contaminant $Fe^{III}$, and (iii) the amplitude of the signals at $g = 7.6$ and 5.5, which originate from the oxidized non-heme iron and oscillate with a period of 2 because of oxidation of the $Fe^{2+}$ by the semiquinone form of PPBQ on the odd-numbered flashes, followed by reduction of $Fe^{3+}$ by $Q_A^-$ on even-numbered flashes (*67*).

The light-minus-dark spectrum showing the multiline signal with better resolution than in Figure 8A is shown in spectrum c of Figure 8B. A narrow structureless signal around $g = 2$ was light-induced together with the multiline signal (spectrum c of Figure 8B). The width of this signal is approximately 8 G, and the *g* value is close to 2.0032. Using the amplitude of the $S_2$-multiline signal in WT′−PSII and that in Y160F−PSII as references, the value of the double integral of the narrow light-induced signal in Y160F−PSII was estimated to be approximately 0.2−0.3% of that of $Tyr_D^{\bullet}$ in WT′−PSII, i.e., arising in about 0.2−0.3% of the centers. The narrow radical and the multiline signal were measured after various dark periods at room temperature following the flash illumination (not shown). The multiline signal decayed with a $t_{1/2} \approx 8$ min. The majority of the narrow signal decayed also with $t_{1/2} \approx 8$ min, while approximately 20−30% of the signal decayed with a $t_{1/2} \approx 1$ min. The possible origins for these narrow signals will be discussed below.

To obtain an $S_2$-multiline signal without interferences from other signals, we developed the following protocol. After the $S_2$-multiline signal was recorded (spectrum c of Figure 8B), the sample was further illuminated by a 820-nm light at 50 K in the EPR cavity. This near-infrared illumination has been shown to convert the spin = $^1/_2$ $S_2$-multiline signal state into an $S \geq {}^5/_2$ spin state characterized by signals around $g = 9$ in cyanobacteria (*56*). Spectrum d of Figure 8B is the difference signal of the before-minus-after 820-nm illumination and corresponds to the $S_2$-multiline signal, which disappeared upon near-infrared illumination. Under these conditions, the $S_2$-multiline signal is free from any radical signals at $g = 2$. Using instrument settings appropriate for radical detection, it was verified that the amplitude of the light-induced $g = 2.0032$ radical signal did not vary upon infrared illumination (not shown). To our knowledge, spectrum d of Figure 8B is the first report of the $S_2$-multiline signal with no interference from any superimposed signal in the central part of the spectrum.

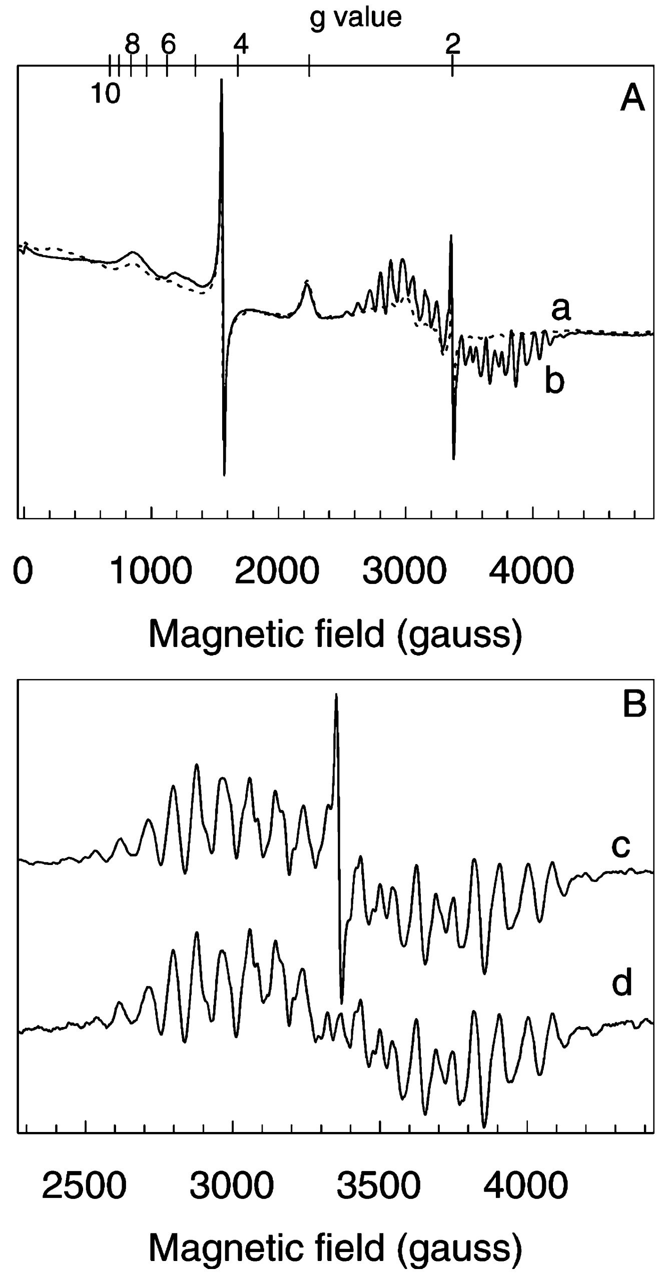


FIGURE 8: EPR spectra in untreated Y160F−PSII. (A) EPR spectra were recorded in dark-adapted Y160F−PSII, i.e., in the $S_1$ state (spectrum a) and after 1 flash given at room temperature (spectrum b). Instrument settings: modulation amplitude, 25 G; microwave power, 20 mW; microwave frequency, 9.4 GHz; modulation frequency, 100 kHz; and temperature, 9 K. [Chl] ≈ 1 mg $mL^{-1}$. (B) Spectrum c is the $S_2$-minus-$S_1$ spectrum. Spectrum d corresponds to a difference spectrum obtained by subtracting the spectrum recorded after a 820 nm illumination at 50 K to that recorded before the near-infrared illumination. Spectra c and d were recorded with modulation amplitude equal to 18 G.

The interest of the new Y160F−PSII preparation in EPR spectroscopy is further demonstrated in the study of a series of so-called split signals (*49*, *51*, *68*, *69*). The 176-G-wide signal induced by near-infrared illumination in the $S_3$ state of the enzyme (*21*, *51*) has been attributed to $S_2Tyr_Z^{\bullet}$ formed by a near-infrared-induced back reaction (*51*). In this state, $Tyr_Z^{\bullet}$ has a spin = $^1/_2$ and $S_2$ is thought to have a spin = $^7/_2$ (*71*). Spectra in Figure 9 show the 176-G-wide signal induced by near-infrared illumination in the $S_3$ state of either WT′−PSII (spectrum a) or Y160F−PSII (spectrum b). To form

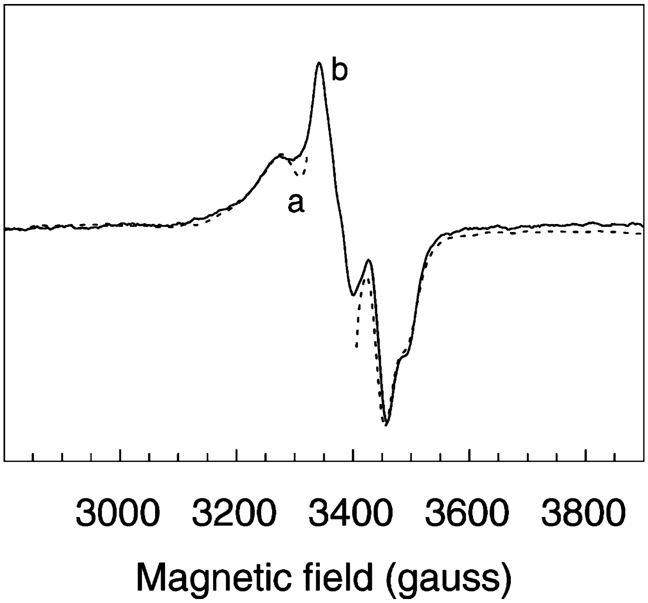


FIGURE 9: Split signal induced by IR light in $S_3$. Spectra light induced by an illumination at 820 nm, at 50 K, of WT′−PSII (spectrum a) and Y160F−PSII (spectrum b). Instrument settings: temperature, 4.2 K; modulation amplitude, 2.8 G; microwave power, 20 mW; microwave frequency, 9.4 GHz; and modulation frequency, 100 kHz. The central part of spectrum a corresponding to the $Tyr_D^•$region was deleted.

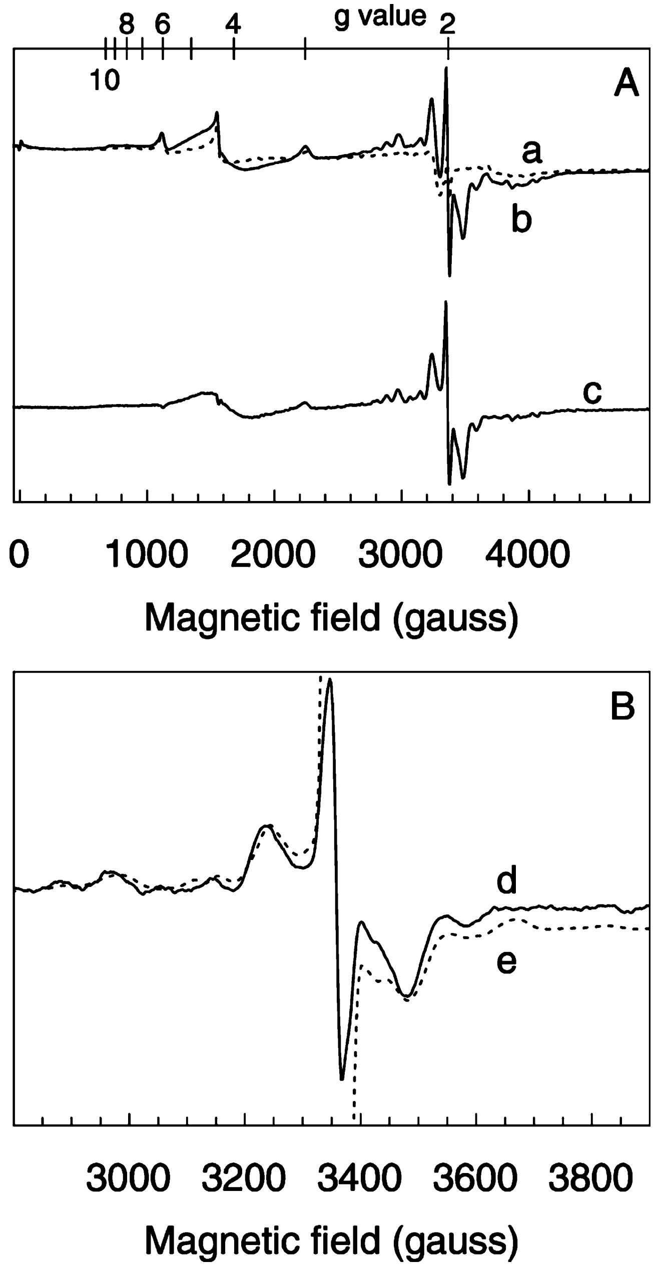


FIGURE 10: EPR spectra in acetate-treated Y160F−PSII. (A) EPR spectra were recorded in dark-adapted Y160F−PSII, i.e., in the $S_1$ state (spectrum a) and after 18 flashes (spaced 500 ms apart), given at room temperature (spectrum b). Instrument settings: modulation amplitude, 18 G; microwave power, 20 mW; microwave frequency, 9.4 GHz; modulation frequency, 100 kHz, and temperature, 9 K. [Chl] $\approx$ 1 mg mL$^{-1}$. Spectrum c is spectrum b minus spectrum a. (B) Light-induced signals recorded on an expanded scale in Y160F−PSII (spectrum d) and WT′−PSII (spectrum e). In spectrum e, the $Tyr_D^•$ region has been deleted.

the $S_3$ state, dark-adapted PSII was illuminated by one preflash and then, after a second dark adaptation for 1 h at room temperature and the addition of PPBQ, the samples were illuminated by 2 additonal flashes. The shape of the infrared-induced signal is similar to that recorded previously with a lower modulation amplitude (*21*) but is shown here without $Tyr_D^•$, which obliterated much of the spectrum.

A further example is the light-induced signal in acetate-treated PSII (*49*). This signal has been attributed to the $S_2$-$Tyr_Z^•$ state in *Synechocystis* sp. PCC 6803 (72). In this case, $S_2$ is attributed to a spin = $^1/_2$ state (*49*, *50*). The split signal in acetate-treated PSII is shown in Figure 10A. Spectrum a was recorded on a dark-adapted sample, and spectrum b was recorded after flash illumination at room temperature. Spectrum c corresponds to the light-minus-dark spectrum. Magnification of spectrum c shows that a small $S_2$-multiline signal and a small signal at $g = 4.25$ were induced by the illumination. The signal at $g = 3.02$ is very likely due to the oxidation of cytochrome *b*559 in a proportion of the centers. Figure 10B compares the split signal in acetate-treated WT′−PSII (spectrum e) to that in Y160F−PSII. Again, the central part of the signal is resolved for the first time. It should be noted that a very small (in less than 1% of the reaction centers) narrow-free radical together with the split signal is also light-induced in this kind of sample. Nevertheless, because of the high microwave power, the high modulation amplitude used, and the very small amount of this light-induced radical, its contribution in spectrum e of Figure 10B is negligible.

## DISCUSSION

We describe the first single amino acid site-directed mutagenesis of PSII in *T. elongatus*, the thermophilic species that has provided the current crystallographic model of the enzyme (*7*). In *T. elongatus*, two genes potentially encode the D2 protein in PSII, *psbD₁* and *psbD₂*. Using the $Tyr_D^•$ EPR signal as a probe, it is shown here that, after introducing the Y160F mutation into D2, a change that affects the growth of the cells particularly under higher light intensities, the expression of the second D2 gene (*psbD₂*) attains ≈50% of that of *psbD₁*. For this reason, the *psbD₂* gene should be removed before mutating both the first D2 gene (*psbD₁*) and the gene for CP43 (*psbC*) in a single step, thereby introducing the Y160F mutation in the D2 protein and adding the His-tag to CP43.

The interruption of the *psbD₂* gene with an antibiotic-resistant gene cassette, rather than its removal, was found to be inappropriate as an experimental system, because the mutations in the $psbD_1$ gene reverted to the normal sequence, the $psbD_2$ gene reverted to its normal length, yet the antibiotic resistance was maintained. These effects lead us to propose that recombination between the two D2 genes can occur in this species.

Under a light intensity equal to 60 $\mu$mol of photons $m^{-2}$ $s^{-1}$, the growth of the Y160F cells was significantly slower than that of the WT′ cells. Therefore, the Y160F mutation creates a new limiting step in the cell growth. Such a slow down for this kind of mutant has already been observed in *Synechocystis* 6803 (*30*, *31*) and ascribed to a decrease in the efficiency of photoactivation, the process by which the Mn cluster is assembled (*31*). This suggestion was recently supported by experimental work in which it was shown that photoactivation occurs with greater efficiency in the *Synechocystis* 6803 WT than in the Y160F mutant (*41*).

The rate of oxygen evolution in Y160F was similar to that in the WT′ in the isolated enzyme. It has been recently shown that the replacement of $Ca^{2+}$ by $Sr^{2+}$ in the $Mn_4CaO_4$ cluster, which resulted in a slow down of oxygen evolution from 1 ms to 5−7 ms, had no effect on the growth rate of the cells (*27*). Therefore, to explain the slower growth of Y160F cells, we have to invoke an effect of the Y160F mutation either on the electron-acceptor side of PSII or on processes different from electron transfer, such as PSII assembly or repair. Thermoluminescent experiments (not shown) indicate that the redox potential of $Q_A^-/Q_A$ is unaffected by the Y160F mutation. This suggests that the slower growth rate is not due to a change in the redox properties of $Q_A^-$. As suggested earlier (*31*, *40*, *41*), a role for $Tyr_D$ in photoactivation of the enzyme seems the most likely explanation for the slow down in growth of the mutant. The longer lag phase before growth takes off in the Y160F mutant might be explained in the same way. When photoactivation is less-efficient, the Mn-free PSII is probably particularly susceptible to photodamage especially when cell densities are low and the light intensity is relatively high.

The flash-induced oxygen evolution measurements (in thylakoid membranes) and the flash-induced absorption changes measured at 292 nm (in isolated PSII) both show that the ratio $S_1/S_0$ is much higher in dark-adapted WT′−PSII than in dark-adapted Y160F−PSII. The lower concentration of the $S_0$ state in WT′ is due to the $S_0Tyr_D^\bullet \rightarrow S_1Tyr_D$ dark reaction (*40*), which obviously cannot occur in the $Tyr_D$-less mutant. In *T. elongatus*, the presence of a significant amount of reduced $Tyr_D$ in the WT′ had little effect on the miss and double-hit parameters, and this contrasts with what is observed in plant PSII. This is due to the rate of the $S_2Tyr_D \rightarrow S_1Tyr_D^\bullet$ (and $S_3Tyr_D \rightarrow S_2Tyr_D^\bullet$) reaction being slow in PSII from *T. elongatus* relative to the dark time between the flashes of a sequence (see below and refs *27* and *73*).

The main reduction reactions in the dark of the enzyme in the $S_3$ state back to the $S_2$ state and of the $S_2$ state back to the $S_1$ state are not significantly modified in the Y160F mutant. It is seems therefore likely that both the $S_1/S_2$ and $S_2/S_3$ couples have the same redox potential in WT′−PSII and Y160F−PSII. The fast phase with a $t_{1/2}$ for $S_3$ decay close to 8 s and that is present in 24% of WT′ reaction centers probably corresponds to the $S_3Tyr_D \rightarrow S_2Tyr_D^\bullet$ reaction. In Y160F thylakoids, we found that $S_1$ could be very slowly reduced ($t_{1/2} \approx 30$ min) into $S_0$ in 20−30% of the centers. The reason of this instability remains to be determined. A similar instability for $S_1$ in a small proportion of WT′−PSII centers would remain not detected because of a compensation by the $S_0Tyr_D^\bullet \rightarrow S_1Tyr_D$ reaction.

Kinetics of $P_{680}^+$ reduction in WT′−PSII and Y160F−PSII exhibit very small differences. As mentioned above, the use of repetitive flash illumination only allowed us to have a global view of the effect of the mutation. A small slow down in the microsecond time scale was nevertheless observed. Changes in this time domain have been proposed to correspond to the reorganization of the hydrogen-bonding network around $Tyr_Z^\bullet$, which in turn could affect the $P_{680}^+$-$Tyr_Z \leftrightarrow P_{680}Tyr_Z^\bullet$ equilibrium (*37*, *74*).

Another effect of the Y160F mutation was a slight acceleration of the fastest part (tens of nanoseconds time scale) of the $P_{680}^+$ reduction. This effect was accounted for by a slightly shorter half-life time (16 ns instead of 19 ns in the WT′) and a slightly larger amplitude (30% instead of 28% in the WT′) of the fastest phase. However, because of the weakness of the effects and the possibility of compensation between phases and between half-life times and amplitudes in multiexponential fits, we would not exclude that either only the half-life time or only the amplitude of the fastest phase was modified by the mutation. A larger amplitude of the fastest phase in the mutant would be most easily explained by a higher average proportion of centers in $S_0$ and $S_1$, to which the fastest phase has been assigned (*35*). A slightly higher proportion of $S_0$ and $S_1$ under repetitive excitation might be supported by our observation of a higher stability of $S_0$ in Y160F−PSII compared to that in WT′−PSII (see Figure 4). An acceleration of the fastest phase of the $P_{680}^+$ reduction may result from a modification of the $P_{680}/P_{680}^+$ properties as discussed below.

Our results on the reduction kinetics of $P_{680}^+$ differ slightly from a comparable study on *Chlamydomonas* in which a qualitatively similar mutation effect was observed in the microsecond scale, but no significant differences were found in the nanosecond time scale (the reported fit parameters of the fastest phase were $t_{1/2} = 14 \pm 3$ ns (37%) in the WT′ and $15 \pm 3$ ns (38%) in Y160F−PSII) (*45*). It is not clear whether the deviation from our results is due to the different species, to the quality or stability of the PSII complexes (PSII from *Chlamydomonas* is more susceptible to damage during isolation than that from *T. elongatus*), or to an insufficient signal-to-noise ratio or time resolution (the data presented in ref *45* were digitized at 20 ns/channel compared to 1 ns/channel in our study).

The difference spectra close to the Soret bleaching of $P_{680}$ upon flash illumination revealed a red shift in WT′−PSII, which oscillated with a period of 4. In Y160F−PSII, this oscillation was attenuated. It has been proposed that $P_{D2}$ absorbs at a slightly higher wavelength than $P_{D1}$, i.e., 436 versus 433 nm (*17*). A small displacement to the right of the $P_{D1}^+P_{D2} \leftrightarrow P_{D1}P_{D2}^+$ equilibrium in the $S_2$ and $S_3$ states when compared to the situation in the $S_0$ and $S_1$ states would account for the oscillating red shift of the spectra observed in WT′−PSII. The results obtained above would suggest that in Y160F−PSII the $P_{D1}^+P_{D2} \leftrightarrow P_{D1}P_{D2}^+$ equilibrium would be less-modified by the redox state of the $Mn_4CaO_4$ cluster. This may occur if in Y160F−PSII the $P_{D1}^+P_{D2} \leftrightarrow P_{D1}P_{D2}^+$

equilibrium in the $S_1$ state was already slightly shifted to the left in the mutant compared to the WT′. Such a shift in favor of $P_{D1}^+P_{D2}$ correlates with the slightly faster reduction of $P_{680}^+$ observed in Y160F−PSII. We may imagine a model in which the absence of $Tyr_D^•$ would slightly affect the position of the His189 (hydrogen bonded to $Tyr_D^•$ in WT′−PSII), which in turn would affect the proton network around $P_{D2}$ and therefore would induce an electrostatic constraint on $P_{D2}$.

The FTIR difference spectrum of $P_{680}^+/P_{680}$ shows that either a carbomethoxy C═O stretch of a Chl molecule or the C═O stretch of a protonated caboxylic acid of the protein side chain downshifted about 10 $cm^{-1}$ upon mutation, although the keto C═O stretching bands of neutral $P_{680}$ and $P_{680}^+$ were virtually unchanged. If the former assignment is the case, then we have to assume that the hydrogen-bonding interaction of the carbomethoxy C═O of $P_{D2}$ with D2-Ser282 (64) becomes stronger by perturbation of the hydrogen-bond network between $P_{D2}$ and $Tyr_D$ upon Y160F mutation. In any case, the FTIR data suggest that the interaction of $P_{680}$ itself or the vicinity of $P_{680}$ is slightly affected by $Tyr_D$ deletion.

The proposed electrostatic influence of $Tyr_D^•(H^+)$ on $P_{680}$, reviewed in ref *32*, is clearly absent. This supports the earlier observations in the less well-characterized and probably less intact material from *Chlamydomonas* (*45*). However, in Mn-depleted PSII, it seems likely that the formation of the $Tyr_D^•$ radical does indeed generate a positive charge, which is maintained in the vicinity of $Tyr_D^•$ at least at higher pH values. The lack of an electrostatic effect in the intact enzyme can be explained if the proton acceptor [the His189 or Gln164, (*7*)] is already protonated under the conditions tested. Because the pH used is thought to be close to the pH in vivo, then clearly, we can conclude that the putative electrostatic effect is not of importance to the normal enzyme function. We cannot rule out an effect at higher pH values, and future studies will focus on the influence of the Y160F mutation at higher pH. It thus remains possible that $Tyr_D$ could have an electrostatic role during photoactivation. Further experiments on Mn-depleted PSII are required to test for such effects.

Overall we have achieved our aim of engineering and isolating a fully intact PSII that lacks the tyrosyl radical $Tyr_D^•$. The absence of the tyrosine has only weak influence on the function of the enzyme other than the specific reactions associated with the redox reactions of $Tyr_D$, i.e., the $Tyr_D^•S_0$−$Tyr_DS_1$ conversion, and the $S_2Tyr_D$−$S_1Tyr_D^•$ and $S_3Tyr_D$−$S_2Tyr_D^•$ conversions. This constitutes the ideal material for a range of spectroscopic studies and particularly for EPR spectroscopy. To show that the EPR signals from PSII can indeed be obtained free of the "$Tyr_D^•$ glitch", we have presented here three demonstration spectra: (i) the multiline signal of the Mn cluster in the $S_2$ state (Figure 8), (ii) the $S_2Tyr_Z^•$ split signal generated when the enzyme is inhibited with acetate (Figure 10), and (iii) another split signal generated by IR illumination of the $S_3$ state (Figure 9).

The central part of the $S_2$-multiline signal reveals, not surprisingly, two more lines. Although these lines will probably have a small influence on the information available from simulations, we commend the new clean signal to the simulators.

A new radical signal was detected in the flash-induced $S_2$ spectrum in Y160F−PSII, and this species behaves as if it was in equilibrium with the spin = $^1/_2$ $S_2$ state giving rise to the multiline signal. Given the very minor influence of $Tyr_D$ removal, it seems likely that the same radical species exists in the WT′−PSII but that until now the $Tyr_D^•$ EPR signal prevented its detection. An estimate of the proportion of centers in which it is detected indicated that the equilibrium would be $S_2$ multiline (>99.8%) ↔ radical (<0.2%). The chemical nature of the radical is not clear. However, the current view of the redox equilibria, $Mn_4^{ox}Tyr_ZP_{680}$ ↔ $Mn_4$-$Tyr_Z^•(H^+)P_{680}$ ↔ $Tyr_ZP_{680}^+$, leads to the prediction that $P_{680}^+$ will be present at a concentration in the order of 0.1% (discussed in ref *75*), i.e., close to the concentration of the radical detected here. Therefore, $P_{680}^+$ might be considered as a possible candidate. Freezing of the sample will have an unpredictable effect on such equilibria; however, if any $P_{680}^+$ becomes trapped, we might expect that the $\beta$-carotene would donate an electron in the 20-ms time scale at a low temperature (*76*, *77*). The $\beta$-carotene cation seems to mediate electron transfer from the cytochrome *b*559 or from $Chl_Z$ when the cytochrome is preoxidized (*77*). In our material, cytochrome *b*559 is in a high redox potential and therefore reduced in the majority of the centers (*28*). However, the radical seen here could reflect the $\beta$-carotene or $Chl_Z$ cation in the fraction of centers in which cytochrome *b*559 is preoxidized.

The signal induced by near-infrared illumination of the $S_3$ state (Figure 9) has the expected pattern of a split signal arising from a radical magnetically interacting with a metal center. By contrast, the light-induced signal in acetate-treated Y160F−PSII differs from what is expected from the simulated spectra (*50*, *78*−*80*). The main surprise is that the signal in Figure 10 exhibits a central line in addition to the expected splitting. Although there are several possible explanations, it seems the simple models applied previously of a spin = $^1/_2$ radical interacting with a noninteger spin system such as the Mn-cluster (spin = $^1/_2$) system generated at the same time should be reassessed at least to describe the situation in a fraction of the centers.

Future EPR studies and simulations will be done using the Y160F−PSII preparation described here. This enzyme, engineered specifically to facilitate such spectroscopic studies, should prove as a new useful tool in work on the enzyme function.

## ACKNOWLEDGMENT

We would like to thank Sun Un for helpful discussions.

## SUPPORTING INFORMATION AVAILABLE

Growth curves, $P_{680}^+$ kinetics, oxygen-release kinetics, and fitting procedures. This material is available free of charge via the Internet at http://pubs.acs.org.

## REFERENCES

1. Debus, R. J. (1992) The manganese and calcium ions of photosynthetic oxygen evolution, *Biochim. Biophys. Acta 1102*, 269−352.
2. Barber, J. (2002) Photosystem II: A multisubunit membrane protein that oxidises water, *Curr. Opin. Struct. Biol. 12*, 523−530.
3. Rutherford, A. W. (1989) Photosystem II, the water-splitting enzyme, *Trends Biochem. Sci. 14*, 227−232.
4. Goussias, C., Boussac, A., and Rutherford, A. W. (2002) Photosystem II and photosynthetic oxidation of water: An overview, *Philos. Trans. R. Soc. London, Ser. B 357*, 1369−1381.

5. Debus, R. J. (2001) Amino acid residues that modulate the properties of tyrosine Y-Z and the manganese cluster in the water oxidizing complex of photosystem II, *Biochim. Biophys. Acta 1503*, 164−186.
6. Diner, B. A. (2001) Amino acid residues involved in the coordination and assembly of the manganese cluster of photosystem II. Proton-coupled electron transport of the redox-active tyrosines and its relationship to water oxidation, *Biochim. Biophys. Acta 1503*, 147−163.
7. Ferreira, K. N., Iverson, T. M., Maghlaoui, K., Barber, J., and Iwata, S. (2004) Architecture of the photosynthetic oxygen-evolving center, *Science 303*, 1831−1838.
8. Peloquin, J. M., and Britt, R. D. (2001) EPR/ENDOR characterization of the physical and electronic structure of the OEC Mn cluster, *Biochim. Biophys. Acta 1503*, 96−111.
9. Robblee, J. H., Cinco, R. M., and Yachandra, V. K. (2001) X-ray spectroscopy-based structure of the Mn cluster and mechanism of photosynthetic oxygen evolution, *Biochim. Biophys. Acta 1503*, 7−23.
10. Svensson, B., Vass, I., and Styring, S. (1991) Sequence analysis of the D1 and D2 reaction center proteins of photosystem II, *Z. Naturforsch., C: Biosci. 46*, 765−776.
11. Nakamura, Y., Kaneko, T., Sato, S., Ikeuchi, M., Katoh, H., Sasamoto, S., Watanabe, A., Iriguchi, M., Kawashima, K., Kimura, T., Kishida, Y., Kiyokawa, C., Kohara, M., Matsumoto, M., Matsuno, A., Nakazaki, N., Shimpo, S., Sugimoto, M., Takeuchi, C., Yamada, M., and Tabata, S. (2002) Complete genome structure of the thermophilic cyanobacterium *Thermosynechococcus elongatus* BP-1, *DNA Res. 9*, 123−130.
12. Hays, A. A., Vassiliev, I. R., Golbeck, J. H., and Debus, R. J. (1999) Role of D1-His190 in the proton-coupled oxidation of tyrosine Y-Z in manganese-depleted photosystem II, *Biochemistry 38*, 11851−11865.
13. Tang, X.-S., Chisholm, D. A., Dismukes, G. C., Brudvig, G. W., and Diner, B. A. (1993) Spectroscopic evidence from site-directed mutants of *Synechocystis* PCC 6803 in favor of a close interaction between histidine 189 and redox-active tyrosine 160, both of polypeptide D2 of the photosystem II reaction center, *Biochemistry 32*, 13742−13748.
14. Campbell, K. A., Peloquin, J. M., Diner, B. A., Tang, X.-S., Chisholm, D. A., and Britt, R. D. (1997) The $\tau$-nitrogen of D2 histidine 189 is the hydrogen bond donor to the tyrosine radical YD of photosystem II, *J. Am. Chem. Soc. 119*, 4787−4788.
15. Faller, P., Goussias, C., Rutherford, A. W., and Un, S. (2003) Resolving intermediates in biological proton-coupled electron transfer: A tyrosyl radical prior to proton movement, *Proc. Natl. Acad. Sci. U.S.A. 100*, 8732−8735.
16. Diner, B. A., Schlodder, E., Nixon, P. J., Coleman, W. J., Rappaport, F., Lavergne, J., Vermaas, W. F. J., and Chisholm, D. A. (2001) Site-directed mutations at D1-His198 and D2-His 97 of photosystem II in *Synechocystis* PCC 6803: Sites of primary charge separation and cation and triplet stabilization, *Biochemistry 40*, 9265−9281.
17. Diner, B. A., and Rappaport, F. (2002) Structure, dynamics, and energetics of the primary photochemistry of photosystem II of oxygenic photosynthesis, *Annu. Rev. Plant Biol. 53*, 551−580.
18. Kok, B., Forbush, B., and McGloin, M. (1970) Cooperation of charges in photosynthetic $O_2$ evolution-I. A linear four step mechanism, *Photochem. Photobiol. 11*, 457−475.
19. Zouni, A., Witt, H. T., Kern, J., Fromme, P., Krauss, N., Saenger, W., and Orth, P. (2001) Crystal structure of photosystem II from *Synechococcus elongatus* at 3.8 Å resolution, *Nature 409*, 739−743.
20. Kamiya, N., and Shen, J.-R. (2003) Crystal structure of oxygen-evolving photosystem II from *Thermosynechococcus vulcanus* at 3.7 Å resolution, *Proc. Natl. Acad. Sci. U.S.A. 100*, 98−103.
21. Boussac, A., Sugiura, M., Inoue, Y., and Rutherford, A. W. (2000) EPR study of the oxygen evolving complex in His-tagged photosystem II from the cyanobacterium *Synechococcus elongatus*, *Biochemistry 39*, 13788−13799.
22. Kuhl, H., Rögner, M., van Breemen, J. F. L., and Boekema E. J. (1999) Localization of cyanobacterial photosystem II donor-side subunits by electron microscopy and the supramolecular organization of photosystem II in the thylakoid membrane, *Eur. J. Biochem. 266*, 453−459.
23. Noguchi, T., and Sugiura, M. (2001) Flash-induced Fourier transform infrared detection of the structural changes during the S-state cycle of the oxygen-evolving complex in photosystem II, *Biochemistry 40*, 1497−1502.
24. Noguchi, T., and Sugiura, M. (2002) Flash-induced FTIR difference spectra of the water oxidizing complex in moderately hydrated photosystem II core films: Effect of hydration extent on S-state transitions, *Biochemistry 41*, 2322−2330.
25. Noguchi, T., and Sugiura, M. (2002) FTIR detection of water reactions during the flash-induced S-state cycle of the photosynthetic water-oxidizing complex, *Biochemistry 41*, 15706−15712.
26. Noguchi, T., and Sugiura, M. (2003) Analysis of flash-induced FTIR difference spectra of the S-state cycle in the photosynthetic water-oxidizing complex by uniform N-15 and C-13 isotope labeling, *Biochemistry 42*, 6035−6042.
27. Boussac, A., Rappaport, F., Carrier, P., Verbavatz, J.-M., Gobin, R., Kirilovsky, D., Rutherford, A. W., and Sugiura, M. (2004) Biosynthetic $Ca^{2+}/Sr^{2+}$ exchange in the photosystem II oxygen evolving enzyme of *Thermosynechococcus elongatus*, *J. Biol. Chem. 279*, 22809−22819.
28. Roncel, M., Boussac, A., Zurita, J. L., Bottin, H., Sugiura, M., Kirilovsky, D., and Ortega, J.-M. (2003) Redox properties of the photosystem II cytochromes *b*559 and *c*550 in the cyanobacterium *Thermosynechococcus elongatus*, *J. Biol. Inorg. Chem. 8*, 206−216.
29. Sugiura, M., and Inoue, Y. (1999) Highly purified thermo-stable oxygen-evolving photosystem II core complex from the thermophilic cyanobacterium *Synechococcus elongatus* having his-tagged CP43, *Plant Cell Physiol. 40*, 1219−1231.
30. Debus, R. J., Barry, B. A., Babcock, G. T., and McIntosh, L. (1988) Site-directed mutagenesis identifies a tyrosine radical involved in the photosynthetic oxygen-evolving system, *Proc. Natl. Acad. Sci. U.S.A. 85*, 427−430.
31. Vermaas, W. F. J., Rutherford, A. W., and Hansson, Ö. (1988) Site-directed mutagenesis in photosystem II of the cyanobacterium *Synechocystis* sp. PCC 6803: Donor D is a tyrosine residue in the D2 protein, *Proc. Natl. Acad. Sci. U.S.A. 85*, 8477−8481.
32. Rutherford, A. W., Boussac, A., and Faller, P. (2004) The stable tyrosyl radical in Photosystem II: Why D? *Biochim. Biophys. Acta 1655*, 222−230.
33. Hoganson, C. W., and Babcock, G. T. (1997) A metalloradical mechanism for the generation of oxygen from water in photosynthesis, *Science 277*, 1953−1956.
34. Vass, I., and Styring, S. (1991) pH-dependent charge equilibria between tyrosine-D and the S states in photosystem II. Estimation of relative midpoint redox potentials, *Biochemistry 30*, 830−839.
35. Brettel, K., Schlodder, E., and Witt, H. T. (1984) Nanosecond reduction kinetics of photooxidized chlorophyll-aII (P-680) in single flashes as a probe for the electron pathway, proton-release, and charge accumulation in the oxygen-evolving complex, *Biochim. Biophys. Acta 766*, 403−415.
36. Schlodder, E., and Meyer, B. (1987) pH dependence of oxygen evolution and reduction kinetics of photooxidized chlorophyll aII (P-680) in photosystem II particles from *Synechococcus* sp., *Biochim. Biophys. Acta 890*, 23−31.
37. Renger, G. (2004) Coupling of electron and proton transfer in oxidative water cleavage in photosynthesis, *Biochim. Biophys. Acta 1655*, 195−204.
38. Westphal, K. L., Lydakis-Simantiris, N., Cukier, R. I., and Babcock, G. T. (2000) Effects of $Sr^{2+}$-substitution on the reduction rates of $Yz^{\bullet}$ in PSII membranes−Evidence for concerted hydrogen-atom transfer in oxygen evolution, *Biochemistry 39*, 16220−16229.
39. Rappaport, F., Blanchard-Desce, M., and Lavergne, J. (1994) Kinetics of electron transfer and electrochromic change during the redox transitions of the photosynthetic oxygen-evolving complex, *Biochim. Biophys. Acta 1184*, 178−192.
40. Styring, S., and Rutherford, A. W. (1987) In the oxygen-evolving complex of photosystem II the $S_0$ state is oxidized to the $S_1$ state by $D^+$ (signal II slow), *Biochemistry 26*, 2401−2405.
41. Ananyev, G. M., Sakiyan, I., Diner, B. A., and Dismukes, G. C. (2002) A functional role for tyrosine-D in assembly of the inorganic core of the water oxidase complex of photosystem II and the kinetics of water oxidation, *Biochemistry 41*, 974−980.
42. Babcock, G. T., and Sauer, K. (1975) Rapid, light-induced transient in electron paramagnetic resonance signal II activated upon inhibition of photosynthetic oxygen evolution, *Biochim. Biophys. Acta 376*, 315−328.
43. Velthuys, B. R., and Visser, J. W. (1975) Reactivation of EPR signal II in chloroplasts treated with reduced dichlorophenol-indophenol. Evidence against a dark equilibrium between two oxidation states of the oxygen evolving system, *FEBS Lett. 55*, 109−112.

44. Messinger, J., and Renger, G. (1993) Generation, oxidation by the oxidized form of the tyrosine of polypeptide D2, and possible electronic configuration of the redox states $S_0$, $S_{-1}$, and $S_{-2}$ of the water oxidase in isolated spinach thylakoids, *Biochemistry 32*, 9379−9386.
45. Jeans, C., Chilsta, J., Ray, N., Hausin, S., Minagawa, J., Nugent, J. H. A., and Klug, D. R. (2002) Replacement of tyrosine D with phenylalanine affects the normal proton-transfer pathways for the reduction of $P_{680}(+)$ in oxygen-evolving photosystem II particles from *Chlamydomonas*, *Biochemistry 41*, 15754−15761.
46. Britt, R. D., Campbell, K. A., Peloquin, J. M., Gilchrist, M. L., Aznar, C. P., Dicus, M. M., Robblee, J., and Messinger, J. (2004) Recent pulsed EPR studies of the photosystem II oxygen-evolving complex: Implications as to water oxidation mechanisms, *Biochim. Biophys. Acta 1655*, 158−171.
47. Carrell, T. G., Tyryshkin, A. M., and Dismukes, G. C. (2001) An evaluation of structural models for the photosynthetic water-oxidizing complex derived from spectroscopic and X-ray diffraction signatures, *J. Biol. Inorg. Chem. 7*, 2−22.
48. Blondin, G., Davydov, R., Philouze, C., Charlot, M. F., Styring, S., Akermark, B., Girerd, J.-J., Boussac, A. (1997) Electron paramagnetic resonance study of the $S = {}^1/_2$ ground state of a radiolysis-generated manganese(III)−manganese(IV)$_3$ form of $[Mn^{IV}{}_4O_6(bipy)_6]^{4+}$ (bipy = 2,2′-bipyridine). Comparison with the photosynthetic oxygen evolving complex, *J. Chem. Soc., Dalton Trans. 21*, 4069−4074.
49. Szalai, V. A., and Brudvig, G. W. (1996) Formation and decay of the S3 EPR signal species in acetate-inhibited photosystem II, *Biochemistry 35*, 1946−1953.
50. Dorlet, P., Boussac, A., Rutherford, A. W., and Un, S. (1999) Multifrequency high-field EPR study of the interaction between the tyrosyl Z radical and the manganese cluster in plant photosystem II, *J. Phys. Chem. B 103*, 10945−10954.
51. Ioannidis, N., and Petrouleas, V. (2000) Electron paramagnetic resonance signals from the S3 state of the oxygen-evolving complex. A broadened radical signal induced by low-temperature near-infrared light illumination, *Biochemistry 39*, 5246−5254.
52. Béal, D., Rappaport, F., and Joliot, P. (1999) A new high-sensitivity 10-ns time-resolution spectrophotometric technique adapted to in vivo analysis of the photosynthetic apparatus, *Rev. Sci. Instrum. 70*, 202−207.
53. Lavorel, J. (1978) Matrix analysis of the oxygen evolving system of photosynthesis, *J. Theor. Biol. 57*, 171−185.
54. Lavergne, J. (1987) Optical-difference spectra of the S-state transitions in the photosynthetic oxygen-evolving complex, *Biochim. Biophys. Acta 894*, 91−107.
55. Lavergne, J. (1991) Improved UV−visible spectra of the S-transitions in the photosynthetic oxygen-evolving system, *Biochim. Biophys. Acta 1060*, 175−188.
56. Boussac, A., Kuhl, H., Un, S., Rögner, M., and Rutherford, A. W. (1998) Effect of near-infrared light on the $S_2$-state of the manganese complex of photosystem II from *Synechococcus elongatus*, *Biochemistry 37*, 8995−9000.
57. Kerfeld, C. A., Yoshida, S., Tran, K. T., Yeates, T. O., Cascio, D., Bottin, H., Berthomieu, C., Sugiura, M., and Boussac, A. (2003) The 1.6 Å resolution structure of Fe-superoxide dismutase from the thermophilic cyanobacterium *Thermosynechococcus elongatus*, *J. Biol. Inorg. Chem. 8*, 707−714.
58. Kerfeld, C. A., Sawaya, M. R., Bottin, H., Tran, K. T., Sugiura, M., Cascio, D., Desbois, A., Yeates, T. O., Kirilovsky, D., and Boussac, A. (2003) Structural and EPR Characterization of the soluble form of Cytochrome *c*-550 and of the *psbV2* gene product from the cyanobacterium *Thermosynechococcus elongatus*, *Plant Cell Physiol. 44*, 697−706.
59. Bustos, S. A., and Golden, S. S. (1992) Light-regulated expression of the psbD gene family in *Synechococcus* sp. strain PCC 7942: Evidence for the role of duplicated psbD genes in cyanobacteria, *Mol. Gen. Genet. 232*, 221−230.
60. Vermaas, W. F. J., Renger, G., Dohnt, G. (1984) The reduction of the oxygen-evolving system in chloroplasts by thylakoid components, *Biochim. Biophys. Acta 764*, 194−202.
61. Lavorel, J. (1992) Determination of the photosynthetic oxygen release time by amperometry, *Biochim. Biophys. Acta 1101*, 33−40.
62. Noguchi, T., Tomo, T., and Inoue, Y. (1998) Fourier transform infrared study of the cation radical of $P_{680}$ in the photosystem II reaction center: Evidence for charge delocalization on the chlorophyll dimer, *Biochemistry 37*, 13614−13625.
63. Breton, J., Hienerwadel, R., and Nabedryk, E. (1997) FTIR difference spectrum of the photooxidation of the primary electron donor of photosystem II, in *Spectroscopy of Biological Molecules: Modern Trends* (Carmona, P., Navarro, R., and Hernanz, A., Eds.) pp 101−102, Kluwer Academic Publishers, Dordrecht, The Netherlands.
64. Sarcina, M., Breton, J., Nabedryk, E., Diner, B. A., and Nixon, P. J. (1998) FTIR studies on the $P_{680}$ cation and triplet states in WT and mutants PSII reaction centres of *Synechocystis* 6803, in *Photosynthesis: Mechanisms and Effects* (Garab, G., Ed.) Vol. 2, pp 1053−1056, Kluwer Academic Publishers, Dordrecht, The Netherlands.
65. Nabedryk, E., Leonhard, M., Mäntele, W., and Breton, J. (1990) Fourier transform infrared difference spectroscopy shows no evidence for an enolization of chlorophyll a upon cation formation either in vitro or during P700 photooxidation, *Biochemistry 29*, 3242−3247.
66. Dioumaev, A. K., and Braiman, M. S. (1995) Modeling vibrational spectra of amino acid side chains in proteins: The carbonyl stretch frequency of buried carboxylic residues, *J. Am. Chem. Soc. 117*, 10572−10574.
67. Zimmermann, J.-L., and Rutherford, A. W. (1986) Photoreductant-induced oxidation of $Fe^{2+}$ in the electron-acceptor complex of photosystem II, *Biochim. Biophys. Acta 851*, 416−423.
68. Boussac, A., Zimmermann, J.-L., and Rutherford A. W. (1989) EPR signals from modified charge accumulation states of the oxygen evolving enzyme in $Ca^{2+}$-deficient photosystem II, *Biochemistry 28*, 8984−8989.
69. Boussac, A., Zimmermann, J.-L., Rutherford, A. W., and Lavergne, J. (1990) Histidine oxidation in the oxygen evolving enzyme, *Nature 347*, 303−306.
70. Ioannidis, N., Nugent, J. H. A., and Petrouleas, V. (2002) Intermediates of the S3 state of the oxygen-evolving complex of photosystem II, *Biochemistry 41*, 9589−9600.
71. Sanakis, Y., Ioannidis, N., Sioros, G., and Petrouleas, V. (2001) A novel $S = {}^7/_2$ configuration of the Mn cluster of photosystem II, *J. Am. Chem. Soc. 123*, 10766−10767.
72. Tang, X. S., Randall, D. W., Force, D. A., Diner, B. A., and Britt, R. D. (1996) Manganese-tyrosine interaction in the photosystem II oxygen-evolving complex, *J. Am. Chem. Soc. 118*, 7638−7639.
73. Isgandarova, S., Renger, G., and Messinger, J. (2003) Functional differences of photosystem II from *Synechococcus elongatus* and spinach characterized by flash induced oxygen evolution patterns, *Biochemistry 42*, 8929−8938.
74. Rappaport, F., Porter, G., Barber, J., Klug, D., and Lavergne, J. (1995) Reinvestigation of the phases of reduction of $P_{680}{}^+$ in the microsecond time domain, in *Photosynthesis: From Light to Biosphere* (Mathis, P., Ed.) pp 345−348, Kluwer Academic Publishers, Dordrecht, The Netherlands.
75. Rappaport, F., Guergova-Kuras, M., Nixon, P. J., Diner, B. A., and Lavergne, J. (2002) Kinetics and pathways of charge recombination in photosystem II, *Biochemistry 41*, 8518−8527.
76. Faller, P., Pascal, A., and Rutherford, A. W. (2001) $\beta$-Carotene redox reactions in photosystem II: Electron-transfer pathway, *Biochemistry 40*, 6431−6440.
77. Hanley, J., Deligiannakis, Y., Pascal, A., and Rutherford, A. W. (1999) Carotenoid oxidation in photosystem II, *Biochemistry 38*, 8189−8195.
78. Lakshmi, K. V., Eaton, S. S., Eaton, G. R., and Brudvig, G. W. (1999) Orientation of the tetranuclear manganese cluster and tyrosine Z in the $O_2$-evolving complex of photosystem II: An EPR study of the S2Yz center state in oriented acetate-inhibited photosystem II membranes, *Biochemistry 38*, 12758−12767.
79. Lakshmi, K. V., Eaton, S. S., Eaton, G. R., Frank, H. A., and Brudvig, G. W. (1998) Analysis of dipolar and exchange interactions between manganese and tyrosine Z in the S2YZ center dot state of acetate-inhibited photosystem II via EPR spectral simulations at X- and Q-bands, *J. Phys. Chem. B 102*, 8327−8335.
80. Peloquin, J. M., Campbell, K. A., Randall, D. W., Evanchik, M. A., Pecoraro, V. L., Armstrong, W. H., and Britt, R. D. (2000) Mn-55 ENDOR of the S-2-state multiline EPR signal of photosystem II: Implications on the structure of the tetranuclear Mn cluster, *J. Am. Chem. Soc. 122*, 10926−10942.


BI048732H

## Supplementary material

**Site-directed mutagenesis of *Thermosynechococcus elongatus* photosystem II: the O2 evolving enzyme lacking the redox active tyrosine D**

Miwa Sugiura, Fabrice Rappaport, Klaus Brettel, Takumi Noguchi, A. William Rutherford and Alain Boussac

I) Fitting procedure of the flash-induced absorption changes at 292 nm.

For technical reasons the analytic laser flash had a small actinic effect. To partially take into account this effect, the data were fitted using a double hit parameter different from zero. The two parameters, $\alpha$ (miss) and $\beta$ (double hit), can be calculated without the knowledge of the individual extinction coefficient $\Delta\varepsilon_n$ for each $S_n$ to $S_{n+1}$ state transition by using the following expressions (53-55):

**[S1]** $(Y_{i+4}-Y_i) - \sigma_1(Y_{i+3}-Y_i) + \sigma_2(Y_{i+2}-Y_i) - \sigma_3(Y_{i+1}-Y_i) = 0$

In which $Y_i$ is a linear combination of the concentration of the $S_n$-states at flash *i*. Here, the $Y_i$ corresponded to the $\Delta I/I$ measured on each flash of the sequences in Figure 5. And:

**[S2]** $\sigma_1 = 4\alpha$

**[S3]** $\sigma_2 = 6\alpha^2-2\beta^2$

**[S4]** $\sigma_3 = 4[\alpha^3-\alpha\beta^2+\beta(1-\alpha-\beta)^2]$

The parameters $\alpha$ and $\beta$ were varied to minimize the left-hand part of equation [S4].

It seems likely that the 3 differential extinction coefficients, $\Delta\varepsilon_0$, $\Delta\varepsilon_1$, $\Delta\varepsilon_2$ (corresponding to the $S_0 \rightarrow S_1$, $S_1 \rightarrow S_2$ and $S_2 \rightarrow S_3$ transitions, respectively) are similar in WT'-PSII and inY160F-PSII, therefore we estimated *i*) the relative proportion of the $S_0$- and $S_1$-states both in dark-adapted WT'- and Y160F-PSII and *ii*) the differential extinction coefficients $\Delta\varepsilon_0$, $\Delta\varepsilon_1$, $\Delta\varepsilon_2$, by doing a global fit of the two sequences in Figure 5. The fitting procedure used was based on that developed by Lavergne (54, 55). First, the relative proportion of each S-state ($S_n$) in WT'- and Y160F-PSII was computed upon each flash *i* of a sequence by using the $\alpha$ and $\beta$ parameters determined above and equations [1] and [2] in which arbitrary starting values for $S_1$ and $S_0$ were introduced. Then, the 3 transition weights, $T_0(i)$, $T_1(i)$, $T_2(i)$ were computed upon each flash of the sequence (54, 55):

**[S5]** $T_0(i) = S_0(i\text{-}1) - S_0(i)$

**[S6]** $T_1(i) = T_0(i) + S_1(i\text{-}1) - S_1(i)$

**[S7]** $T_2(i) = T_1(i) + S_2(i\text{-}1) - S_2(i)$

An then, the $\Delta I/I$ upon each flash of the sequence were calculated by using 3 arbitrary starting values for $\Delta\varepsilon_0$, $\Delta\varepsilon_1$ and $\Delta\varepsilon_2$.

**[S8]** $(\Delta I/I)(i) = \sum_{i=0}^{2} \Delta\varepsilon_i \, T_n(i)$

Adjustment of $(\Delta I/I)(i)$ computed from equation [S8] to the experimental $\Delta I/I$ values was done by varying the $S_1$ and $S_0$ proportions in WT'-PSII and Y160F-PSII and the 3 coefficients $\Delta\varepsilon_0$, $\Delta\varepsilon_1$ and $\Delta\varepsilon_2$. Data from the first flash which include centers blocked upon formation of $S_2$ were not taken into account in the fitting procedure (55).

II) Kinetics of the $S_n$-states in the dark.

The flash-induced $O_2$ evolution patterns were measured and fitted (by using equations [1] and [2] in the manuscript), using the same $\alpha$ and $\beta$ values determined from the flash-induced oxygen evolution pattern (Figure 3), and the $S_3/S_2/S_1/S_0$ contents after each dark-time were deduced. For each sample, the concentration of $S_3$, $S_2$ and $S_1$ versus the dark-time after 2 flashes were fitted globally. A bi-exponential decay was used for the transition from $S_3$ to $S_2$. The fits also included a proportion of centers in $S_2$ (which deactivated to form $S_1$ during the experiment) and a small proportion of centers in $S_1$ after the second flash. We neglected a possible fraction of centers in the $S_2Tyr_D$-state after the second flash which would react to give the $S_1Tyr_D^{\bullet}$-state during the dark-period. The equations used are listed below:

**[S9]** $[S_3]_t = [S_3]_{t=0}\cdot(p\cdot\exp(-k_1\cdot t)+(1-p)\cdot\exp(-k_2\cdot t))$

**[S10]** $[S_2]_t = [S_2]_{t=0}\cdot\exp(-k_3\cdot t)+p\cdot[S_3]_{t=0}\cdot(k_1/(k_3-k_1)\cdot(\exp(-k_1\cdot t)-\exp(-k_3\cdot t)))+$
$(1-p)\cdot[S_3]_{t=0}\cdot(k_2/(k_3-k_2)\cdot(\exp(-k_2\cdot t)-\exp(-k_3\cdot t)))$

**[S11]** $[S_1]_t = [S_1]_{t=0}+[S_2]_{t=0}\cdot(1-\exp(-k_3\cdot t))+([S_3]_{t=0}-[S_3]_t-(p\cdot[S_3]_{t=0}\cdot(k_1/(k_3-k_1)\cdot(\exp(-k_1\cdot t)-$
$\exp(-k_3\cdot t)))+(1-p)\cdot[S_3]_{t=0}\cdot(k_2/(k_3-k_2)\cdot(\exp(-k_2\cdot t)-\exp(-k_3\cdot t)))))$

$[S_3]_t$, $[S_2]_t$, $[S_1]_t$ were the experimental points and $[S_3]_{t=0}$, $[S_2]_{t=0}$, $[S_1]_{t=0}$, $k_1$, $k_2$, $k_3$, $p$. the variables to adjust.

III) Growth curves of cells.

Growth curves of cells. In Panel A, light intensity was ≈ 60 µmol photons·$m^2$·$s^{-1}$ and in Panel B, light intensity was ≈ 15 µmol photons·$m^2$·$s^{-1}$. WT' cells (○),WT(Δ*psbD₂*) cells (+), Y160F cells (●).

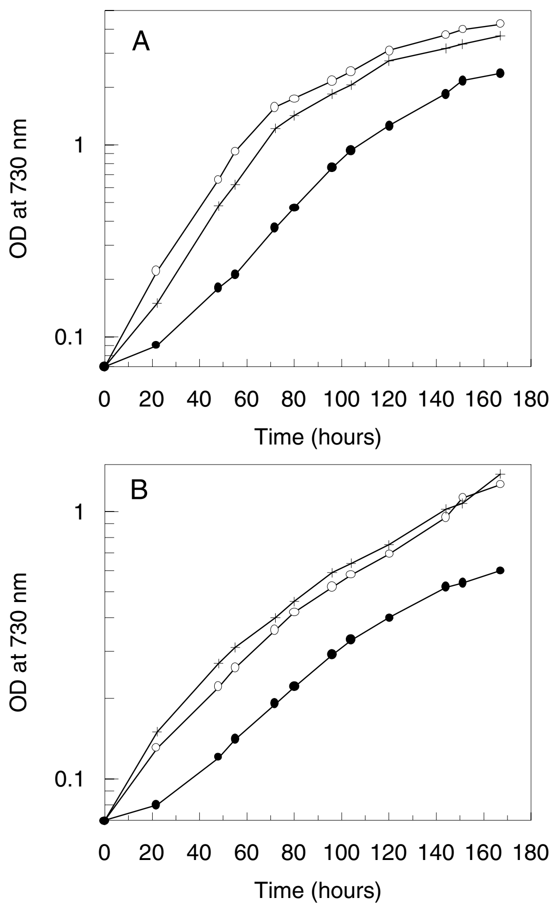

IV) Kinetics of the oxygen release.

Measurements were done after the third flash given on WT'-thylakoids (trace a) and Y160F-thylakoids (trace b) dark-adapted for 1 hour on the bare platinum electrode. Other experimental conditions as in Figure 3 except a 10 times faster time-scale. The smaller amplitude of the signal observed for the Y160F mutant mainly arose from the smaller ratio $S_1/S_0$ in the dark-adapted state.

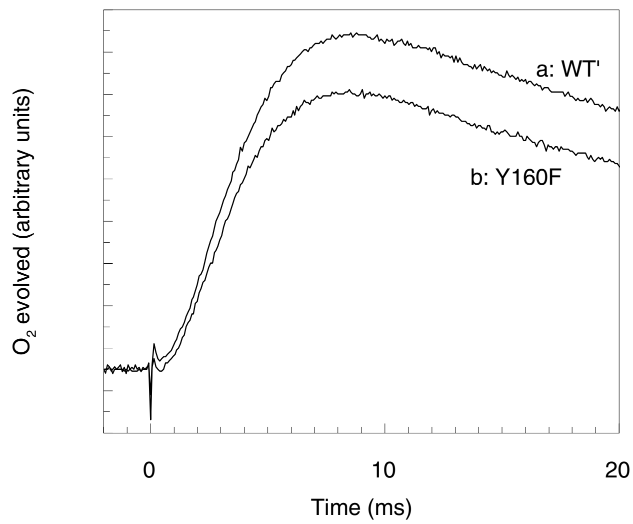

V) Kinetics of $P_{680}^+$ reduction.

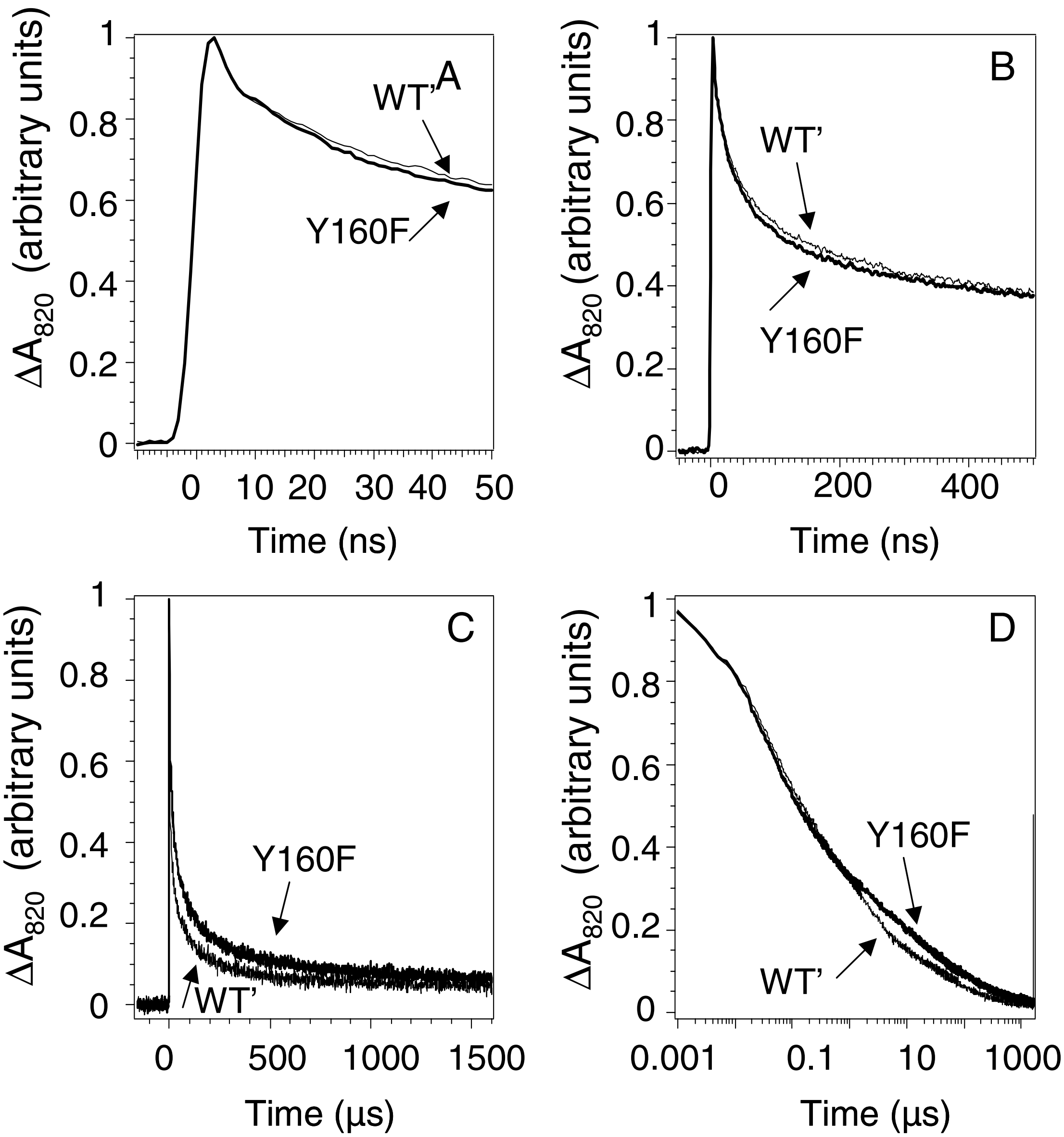


Flash-induced absorption changes at 820 nm measured with a time resolution of about 3 ns on WT'-PSII and Y160F-PSII. Photo-oxidation of $P_{680}$ is accompanied by a rapid, instrument-limited absorption increase followed by a decay corresponding to the reduction of $P_{680}^+$ in the dark. Panels A, B and C correspond to three different time-scales and Panel D shows the full decay of on a logarithmic time-scale. The traces are averages of 16 signals measured under repetitive excitation, and were normalized for the ease of comparison.

Qualitative inspection of the traces reveals that the Y160F mutation has only small effects on $P_{680}^{+}$ reduction, namely a slight acceleration in the tens of nanoseconds scale and some slowing in a scale from a few microseconds to a few hundreds of microseconds. These deviations were reproducible between independent experiments.

Normalized flash-induced absorption transients at 820 nm in WT'-PSII (thick lines) and Y160F-PSII (thin lines). Panels A, B, and C show the absorption transients on different time-ranges. Panel D shows the full decay on a logarithm time-scale. Excitation energy, ~ 4 $mJ \cdot cm^{-2}$. One arbitrary unit corresponds to an absorption change of 15.3 $10^{-3}$ OD for WT'-PSII ([Chl] ≈ 100 $\mu g \cdot ml^{-1}$) and 18.4 $10^{-3}$ OD for Y160F-PSII ([Chl] ≈ 140 $\mu g \cdot ml^{-1}$).

VI) Absorption changes at 439 nm.

Measurements were done 5 ns after flash illumination, in WT'-PSII (—■—) and Y160F-PSII (—■—).

The experimental data were fitted similarly to those at 292 nm by using the parameters listed in the following table. An additional very small offset of –51 $10^{-6}$ accumulated on each flash was added in the fitting of the Y160F data: (---□---) fit of WT'-PSII, (---□---) fit of Y160F-PSII. The green trace (—■—) was calculated with the parameters used to fit the WT'-PSII data excepted the $S_1/S_0$ ratio which was changed to 0.7/0.3 .

| | $S_1/S_0$ | α | β | $\Delta\varepsilon_0$ ($\times10^6$) | $\Delta\varepsilon_1$ ($\times10^6$) | $\Delta\varepsilon_2$ ($\times10^6$) | offset ($\times10^6$) |
|---|---|---|---|---|---|---|---|
| WT'-PSII | 1.0/0.0 | 0.06 | 0.05 | 627 | 2270 | -1004 | -15350 |
| Y160F-PSII | 0.79/0.21 | 0.07 | 0.06 | 533 | 1543 | -1235 | -14978 |

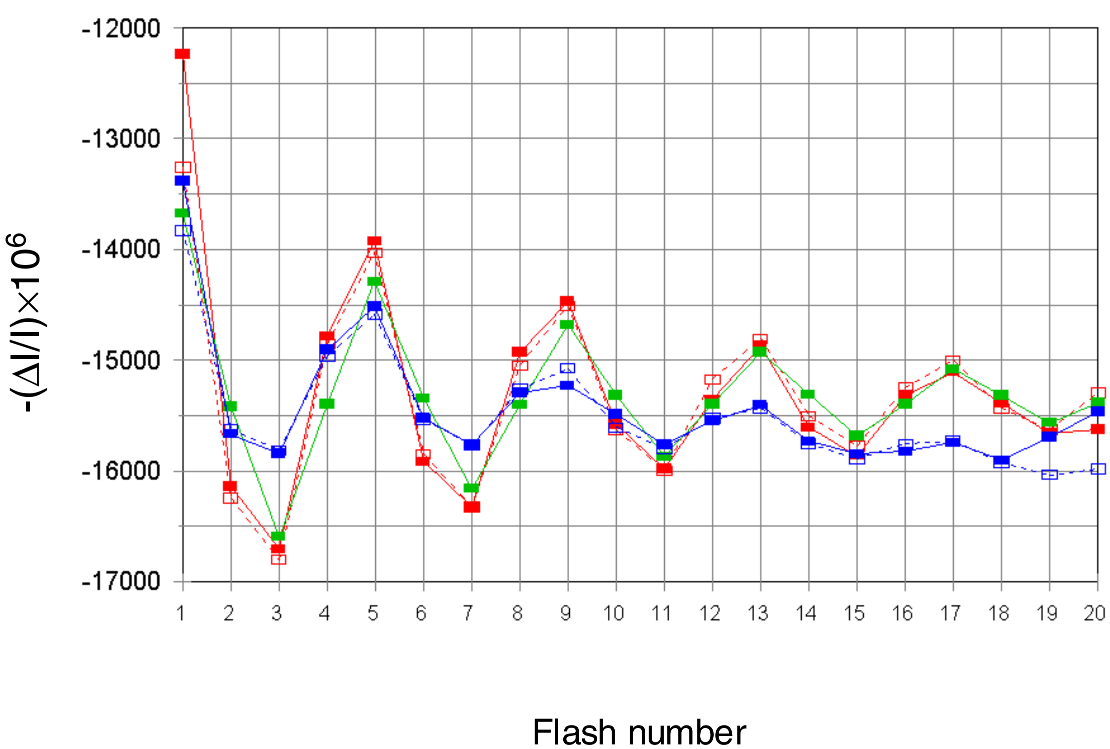

By repeating the procedure described above for each wavelength between 415 nm and 450 nm, it is possible to estimate the 3 extinction coefficients $\Delta\varepsilon_0$, $\Delta\varepsilon_1$ and $\Delta\varepsilon_2$ for all the wavelengths in Figure 6 and then to calculate the absolute difference spectra of the four states $S_0P_{680}^+$ / $S_0P_{680}$, $S_1P_{680}^+$ / $S_1P_{680}$, $S_2P_{680}^+$ / $S_2P_{680}$ and $S_3P_{680}^+$ / $S_3P_{680}$. Briefly, the results are the followings: *i*) the four difference spectra are slightly shifted from the blue to the red with the following order: $S_1P_{680}^+$, $S_0P_{680}^+$, $S_2P_{680}^+$ and $S_3P_{680}^+$ which is consistent with the $S_2$ and $S_3$ being states where a charge accumulation is not compensated by the loss of a proton (39); *ii)* the $S_3P_{680}^+$ *minus* $S_1P_{680}^+$ differential spectrum has a negative peaks at 436 nm (and is positive below 430 nm), *iii*) the $S_1P_{680}^+$ spectrum in Y160F-PSII seems very slightly blue shifted when compared to the $S_1P_{680}^+$ spectrum in WT'-PSII.